Materials Science and Engineering B 192 (2015) 26–51

Contents lists available at ScienceDirect

Materials Science and Engineering B

journal homepage: www.elsevier.com/locate/mseb

Review

# Study of electrical fatigue by defect engineering in organic light-emitting diodes

Andrea Gassmann[a,*], Sergey V. Yampolskii[b], Andreas Klein[c], Karsten Albe[b], Nicole Vilbrandt[d], Oili Pekkola[a], Yuri A. Genenko[b], Matthias Rehahn[d], Heinz von Seggern[a]

[a] Technische Universität Darmstadt, Materials Science and Geoscience Department, Electronic Materials Division, Alarich-Weiss-Str. 2, 64287 Darmstadt, Germany
[b] Technische Universität Darmstadt, Materials Science and Geoscience Department, Materials Modeling Division, Jovanka-Bontschits-Str. 2, 64287 Darmstadt, Germany
[c] Technische Universität Darmstadt, Materials Science and Geoscience Department, Surface Science Division, Jovanka-Bontschits-Str. 2, 64287 Darmstadt, Germany
[d] Technische Universität Darmstadt, Chemistry Department, Ernst Berl Institute for Macromolecular Research, Alarich-Weiss-Str. 4, 64287 Darmstadt, Germany

ARTICLE INFO

*Article history:*
Received 10 June 2014
Received in revised form 4 October 2014
Accepted 24 October 2014
Available online 4 November 2014

*Keywords:*
PLED
Electrical fatigue
Degradation
Lifetime
PPV
ITO

ABSTRACT

In this work the current knowledge on the electrical degradation of polymer-based light-emitting diodes is reviewed focusing especially on derivatives of poly(*p*-phenylene-vinylene) (PPV). The electrical degradation will be referred to as electrical fatigue and is understood as mechanisms, phenomena and material properties that change during continuous operation of the device at constant current. The focus of this review lies especially on the effect of chemical synthesis on the transport properties of the organic semiconductor and the device lifetimes. In addition, the prominent transparent conductive oxide indium tin oxide as well as $In_2O_3$ will be reviewed and how their properties can be altered by the processing conditions. The experiments are accompanied by theoretical modeling shining light on how the change of injection barriers, charge carrier mobility or trap density influence the current–voltage characteristics of the diodes and on how and which defects form in transparent conductive oxides used as anode.



**Contents**



* Corresponding author. Tel.: +49 6151166689; fax: +49 6151166305.
*E-mail address:* gassmann@e-mat.tu-darmstadt.de (A. Gassmann).
*URL:* http://www.sfb595.tu-darmstadt.de/sfb595 (A. Gassmann).

http://dx.doi.org/10.1016/j.mseb.2014.10.014

## 1. Introduction

In the field of organic electronics, organic light-emitting diodes (OLEDs) are nowadays the devices that have already successfully entered the market [1]. Even though the amount of produced organic displays will continuously grow and new application fields will be entered, a lot of processes contributing to the functionality of the devices are still not fully understood and intense research is still ongoing.

Among the variety of organic semiconductors (OSCs), the polymers offer great possibilities in terms of processing: As they are processed from solution, spin coating and printing techniques are envisaged due to their potential low cost production. Nevertheless, most commercial devices that are on the market today are made of low molecular weight compounds that are also known as small molecules [1,2]. For these materials the device performance and lifetime are usually superior to polymeric devices [3] but they have the disadvantage of thermal evaporation processing requiring high vacuum conditions. In order to merge the advantages of both material classes one strategy of the last decade has been to make small molecules solution processable [4–6].

However, polymeric semiconductors are still widely used in organic electronics, making the understanding of the fundamental processes contributing to the functionality of the devices and to their degradation during electrical operation essential. This work does not intend to give a complete and universal overview on device degradation. It attempts to summarize main parts of current knowledge of device degradation in polymer-based organic light-emitting diodes (PLEDs) highlighting especially the results obtained within the present collaborative work covering the whole process chain from materials synthesis, device processing and characterization to device modeling. Taking the results from the different disciplines we want to emphasize that device degradation is a complex subject making the universal understanding of its origins due to the multitude of materials and device geometries challenging.

### 1.1. The structure and functional principle of organic light-emitting diodes

In the most simple organic light-emitting diode, one organic semiconducting layer is sandwiched between two electrodes. During the application of an electric voltage, holes and electrons will be injected from the anode and cathode, respectively. In order to make this charge carrier injection efficient, the involved injection barriers should be as low as possible. This means that the work function of the anode and the highest occupied molecular orbital (HOMO) of the semiconductor as well as the work function of the cathode and the lowest unoccupied molecular orbital (LUMO) should match. For common organic semiconductors the energetic position of the HOMO is around 5 eV and that of the LUMO around 3 eV [7]. The material of choice for the anode is the transparent and conductive Sn-doped indium oxide (ITO) allowing for a good hole injection and for the outcoupling of the generated electroluminescence through the substrate. The electron injecting contact consists of a low work function material like an alkaline or earth alkaline metal. In order to produce light, the injected charge carriers need to be transported in the electric field until they meet forming an exciton. This quasi-particle can diffuse within its lifetime until it decays radiatively, thereby producing light that is emitted, or non-radiatively thereby producing heat.

In this review PLEDs have been investigated consisting of a single layer of fluorescent poly(*p*-phenylene-vinylene) (PPV) derivatives synthesized in our own labs in order to keep control over the quality of the material and the defect contents. The polymers under consideration are red-emitting poly[2-(2′-ethylhexyloxy)-5-propoxy-1,4-phenylene-vinylene] ($OC_3C_8$-PPV), poly[2,5-bis(2′-ethylhexyloxy)-1,4-phenylene-vinylene] ($OC_8C_8$-PPV) and poly[2-(3′,7′-dimethyloctyloxy)-5-methoxy-1,4-phenylene-vinylene] ($OC_1C_{10}$-PPV) whose chemical structures are depicted in Fig. 1. The class of the PPVs has been employed as model system to systematically study the impact of chemical or structural defects in the organic semiconductor on the performance and degradation of the produced light-emitting diodes.

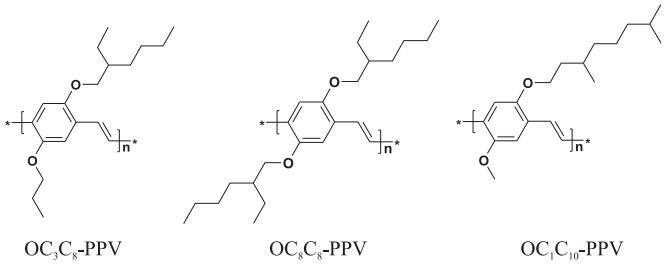


**Fig. 1.** Chemical structures of the investigated organic semiconductors.

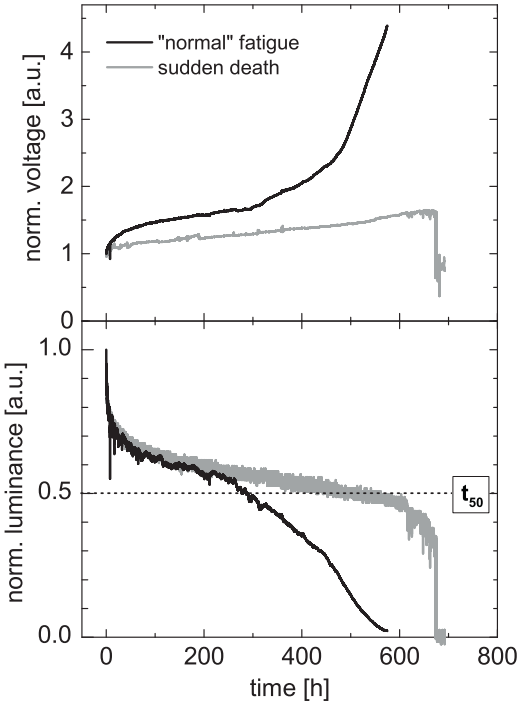


**Fig. 2.** Phenomenology of electrical fatigue in PPV-based devices operated at a constant current density (here 50 mA/cm$^2$). Luminance and driving voltage have been normalized to the initial values.

ITO is employed as anode in combination with a poly(3,4-ethylenedioxythiophene) poly(styrene sulfonate) (PEDOT:PSS) hole injection layer. A calcium layer serves as cathode that is capped with an aluminum overlayer to avoid oxidation. The devices are prepared and characterized in a glove box with inert nitrogen atmosphere.

### 1.2. The phenomenology of electrical degradation

Device degradation can have several appearances, therefore it will be first defined which different types can be distinguished. The device degradation addressed here is due to the continuous electrical operation of the PLED and will be referred to as *electrical fatigue*. The *aging* of a device during long term storage will not be in the focus of this contribution. In this work the diodes are electrically fatigued by the application of a constant current density as is common practice in the field [8–13]. Usually, an increase in voltage and a homogeneous decrease of the intensity of the emitted light with operation time are observed as shown in Fig. 2. This phenomenon is often referred to as *intrinsic degradation* of the devices [7,8,14,15]. To characterize the state of the fatigue, the $t_{50}$ lifetime is determined, i.e. the time after which the initial luminance decreased to half of its initial value.

Another manifestation of fatigue can be the inhomogeneous decrease of the luminance due to the formation of non-emissive regions or *dark spots*. Their presence is usually related to the oxidation of the cathode by moisture or oxygen at pinholes or dust particles [9,16,17] and to the delamination of the top electrode [18–20]. It is generally believed that pre-existing structural defects especially at the organic semiconductor/cathode interface act as nucleation sites for the dark spots, whereas species like water and oxygen mediate their growth. Since all investigations are conducted in inert atmosphere only, this effect is minor and will not be detailed in this work. However, the so-called *sudden death* phenomenon has to be considered. It is the catastrophic failure of the device due to electrical shorts: The driving voltage suddenly drops to very low

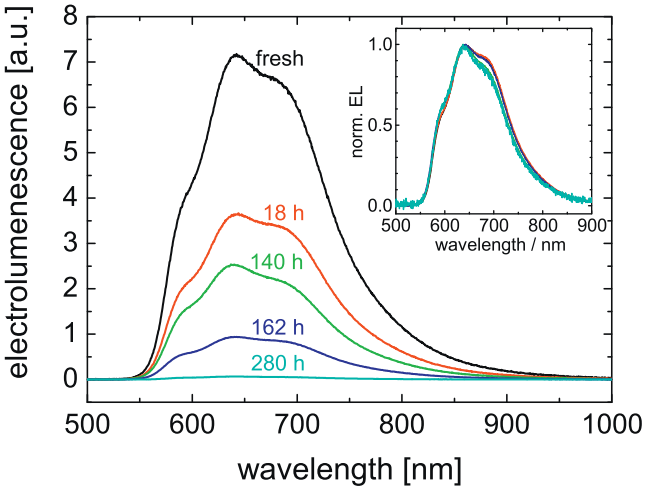


**Fig. 3.** Electroluminescence spectra for fresh and electrically fatigued $OC_3C_8$-PPV OLEDs measured at a constant current density of 10 mA/cm$^2$. The inset shows the same data normalized to the emission maximum.

values[1] while the diode does not emit light any more (see Fig. 2). It is believed that the latter two degradation phenomena can be successfully suppressed by a proper processing and encapsulation of the devices [7–9,14,15] whereas the intrinsic degradation still remains not fully understood.

In our understanding electrical fatigue includes all mechanisms, phenomena and material properties that change during the continuous operation of the device. Consequently, this implicates all physical processes contributing to the functionality of the device like charge carrier injection, charge carrier transport and light generation. In OLEDs these processes are not independent from one another, thereby the change of one process induces in general also other changes. Therefore, it is usually attempted to conduct fatigue experiments in such a way that the specific effect on e.g. the lifetime or the transport properties is investigated preferably without changing other properties.

Yet, this is challenging as it is hardly possible to assign which process contributes to what extent to the fatigue or where it actually occurs in the device. Even though the decrease of the electroluminescence intensity with prolonged operation time is observed homogeneously on the whole active area of the PLED, the here described fatigue is not a global phenomenon per se. The photoluminescence of the PPV derivative that is measured simultaneously with the electroluminescence shows no changes over time indicating that the majority of the polymer molecules is not affected by the continuous electrical operation of the device [21–23]. Additionally, the shape of the electroluminescence spectrum does not change during electrical fatigue experiments, even though the absolute intensity decreases more and more (see Fig. 3). Thus, fatigue is in general a local phenomenon during which presumably only small volumes of the semiconductor are involved. This can be the semiconductor/electrode interfaces that are changed thereby affecting the injection of both charge carrier types. Another possibility is the creation of trap states in the bulk that affect the charge carrier transport properties. It is known from previous work that even small amounts of trap states in the ppm range can alter the charge carrier transport dramatically [24].

[1] These are usually around 2 V for a driving current density of 50 mA/cm$^2$, in opposition to the otherwise measured voltage being ≥5 V depending on the fatigue status of the device.

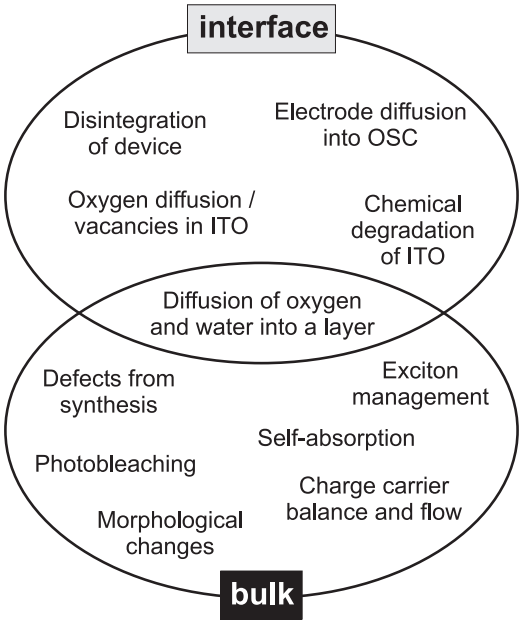


**Fig. 4.** Illustration of in literature and in the present work discussed factors contributing to electrical fatigue of organic light-emitting diodes.

### 1.3. *Possible mechanisms to explain fatigue phenomena*

Within the last decade a considerable amount of research work has been focused on understanding the mechanisms causing degradation in OLEDs. Fig. 4 sums up the most important factors that have been found to contribute to the electric operation-related deterioration of organic light-emitting devices. Here, a classification between bulk and interface processes has been chosen.

The degradation of a device can have extrinsic origins like the diffusion of oxygen or water into the layers. This leads for example to a chemical reaction with the cathode that is usually deposited as the last layer of the device. As a consequence non-emissive dark spots evolve and the whole top electrode might delaminate as mentioned above. Accordingly, active area is lost for light emission as well as active volume for current conduction, leading to an increased driving voltage of the device (at an applied constant current). As aforementioned, these effects can be successively avoided with a proper device processing and hermetic encapsulation.

The origin of intrinsic degradation on the other hand is not so obviously to identify, as intrinsic degradation is strongly material dependent. In general, highly efficient OLEDs have a multilayer setup to ensure optimal charge carrier injection and conduction, carrier balance and recombination at a certain region in the device. Consequently, the functionality of the device is ensured by the interplay between many different organic semiconductors, emitters and possibly also metal oxides used as dopants or injection layers. The chemical degradation of small molecules in the bulk has been reviewed recently by Schmidbauer et al. [8] who stated that the dissociation of weak bonds and the following radical formation leads to chemical reactions with neighboring molecules. Also other groups, e.g. [25–29], support these findings with similar results. The defects, generated as a result of the chemical degradation, affect the charge carrier transport properties as well as the luminescence properties of the OLED negatively. Apart from these defects in the bulk of the semiconductor, interface reactions at the electrodes might take place leading to the formation of electronic states in the energy gap that can be filled [30–36] or to the formation of reaction products [23,37] both deteriorating or impeding charge carrier injection and as a consequence the charge carrier balance in the device. Further processes affecting the functionality of OLEDs are photodegradation, photooxidation and photobleaching occurring under illumination. Here a decrease of the emission intensity is observed [38–43] or also wavelength-shifted emission features changing the overall color of the device [44,45]. Additionally, the light emission intensity is influenced by the presence of quenching sites [14,40,46,47]. Recently, it has also been found that the self-absorption of the light generated by the PLED influences its charge carrier transport properties by prolonging the holes' transit time [22], i.e. decreasing their mobility as will be discussed in Section 4. This finding is attributed to the formation of trap states.

In the case of electrically fatigued devices trap-formation could be confirmed for different materials and using various methods [13,22,48–51]. A consequence might be the broadening of the density of states or the introduction of a trap state density both resulting in lower effective charge carrier mobilities and possibly also a transition to a dispersive transport.

In order to increase the yield and to enhance the lifetime of OLEDs, PEDOT:PSS has been introduced and been frequently used as hole injection layer [9,52–55]. One additional benefit of this interlayer is that the ITO anode is not in direct contact with the organic semiconductor. Therefore, PEDOT:PSS takes also the role of a buffer layer for possibly out-diffusing oxygen from ITO. Yet, it cannot block the out-diffusion of indium that has been observed to penetrate deeply into the organic layer(s) [54,56,57]. Despite of this, indium migration seems to play only a minor role in the fatigue of small-molecular or polymeric OLEDs. Most of today's devices still contain ITO and show decent or very good lifetimes. On the other hand more and more investigations reveal that PEDOT:PSS also introduces problems for the devices [58–60]. This motivates current research on replacing PEDOT:PSS by alternative materials, e.g. transition metal oxides.

For a more detailed analysis of interfacial degradation in organic devices, the review by Turak [58] is recommended.

## 2. Chemical defect engineering in polymeric semiconductors

Since the discovery of electroluminescence, polymer-based semiconductors are widely investigated. They are promising candidates for different kinds of (opto)electronic applications [61–68]. In the following section investigations on the synthesis of two polymeric semiconductors will be reflected: Iridium-functionalized polyfluorenes (PFs) and PPVs. Both types of materials have proven to be useful emitters in OLEDs that can be achieved either by polycondensation [69–75,77,78] or with the help of precursor methods [76,79–81].

Drawbacks of most synthetic methods are the formation of constitutional defects, reactive polymer end-groups, in some cases metal-catalyst impurities and low-molecular weight materials [82,83]. Those defects and impurities are known to limit lifetime and efficiency of resulting devices considerably. While constitutional defects can interrupt the conjugation and therefore the charge carrier transport along the polymeric backbone (for example the exomethylene defect in polymers synthesized via the Heck reaction), catalyst impurities can cause short-circuit in the devices [82]. In addition, materials of low molar mass bear the risk of a high level of reactive end-groups and poor physical properties, i.e. film formation.

Therefore, methods were investigated to reduce or avoid those defects and impurities completely. Subsequently, the polyfluorene derivatives are prepared via the Suzuki- [69–71] and Yamamoto-approaches [72] whereas the PPVs are prepared via the Heck- [73–75] and the Gilch-methods [76].

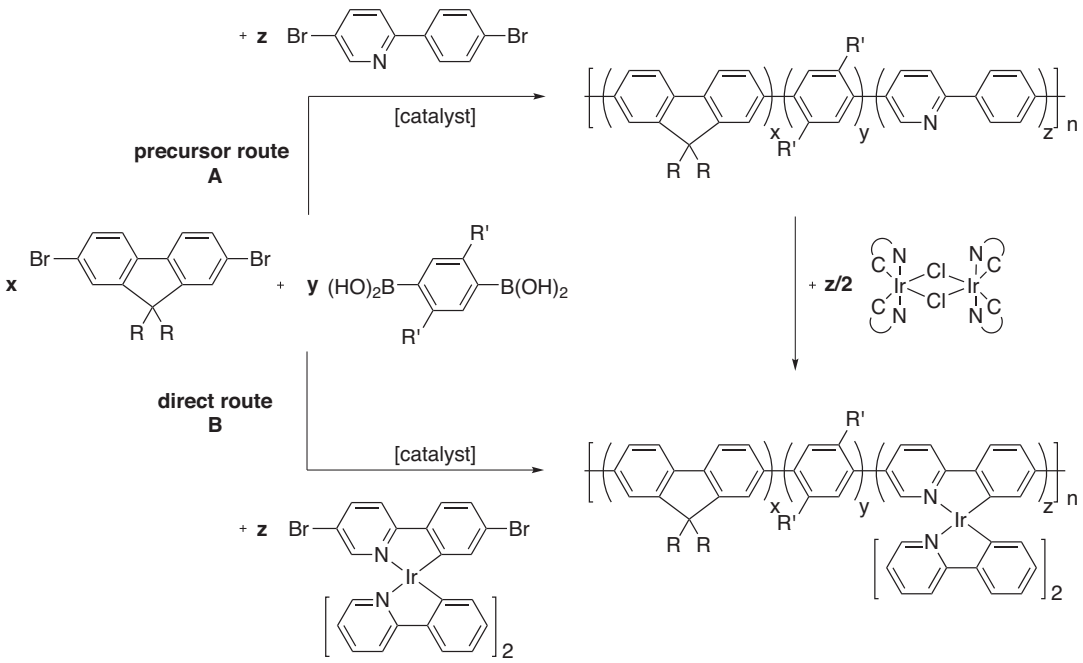


**Fig. 5.** Synthesis of iridium-functionalized polyfluorenes via the Suzuki and Yamamoto method: precursor synthesis (route A) and direct synthesis (route B). Suzuki method: $x = 1.0 \ldots 0.9$, $y = x + z = 1$, $z = 0.0 \ldots 0.1$, catalyst = tetrakis(triphenylphosphine) palladium(0) ($Pd(PPh_3)_4$); Yamamoto method: $x = 1.0 \ldots 0.9$, $y = 0$, $z = 0.0 \ldots 0.1$, catalyst = bis(1,5-cyclooctadiene) nickel(0) ($Ni(COD)_2$) + 2,2′-bipyridine.

### 2.1. Suzuki and Yamamoto synthesis of polyfluorenes

For the realization of blue emission in OLEDs, polyfluorenes are considered a very useful class of materials [84–86]. Their synthesis can be achieved via step-growth processes. The target of our investigation was to realize the synthesis of polyfluorene-containing substituents with heavy-metal atoms like iridium to create triplet emitters [87,88]. The synthesis was achieved via two different approaches, a precursor route A and a direct route B (see Fig. 5).

In both routes the Suzuki and the Yamamoto methods were applied. In case of the precursor route the results showed that the Suzuki method delivers material of high purity. Unfortunately, the coordination of the ligand is not quantitative. For the Yamamoto method the precursor route delivers material of low purity and high amounts of remaining metal catalyst contamination. In case of the direct route the Suzuki method delivers material of low purity and low molecular weight. In contrast, the Yamamoto method leads to polymers of high purity and a considerable constitutional homogeneity [87].

Although the Yamamoto reaction is the method of choice to prepare iridium-functionalized polyfluorene, remaining traces of metal catalyst in the polymer and low degrees of polymerization are still issues in the realization of appropriate lifetimes in OLEDs.

### 2.2. Heck and Gilch synthesis of poly(p-phenylene-vinylene)s

PPVs are another class of promising light-emitting semiconductors whose synthesis can be achieved via different procedures. On the one hand it is possible to receive this material via step-growth processes like the Heck reaction [73–75]. Another possibility uses chain-growth processes like the Gilch method [76].

At first the results for the transition metal catalyzed Heck procedure (see Fig. 6) will be described. Usually, the catalytic system consists of palladium(II)acetate ($Pd(OAc)_2$), triphenylphosphine ($PPh_3$), triethylamine ($Et_3N$) and *N*,*N*-dimethylformamide (DMF) [89]. The resulting material is most likely oligomeric and therefore not suitable for OLEDs. Thus, another much more promising catalyst system has been developed that consists of bis(dibenzylideneacetone)palladium(0) ($Pd(dba)_2$), tri-*tert*-butylphosphine ($P^tBu_3$), diisopropylamine ($NH^iPr_2$) and tetrahydrofuran (THF) [90]. The resulting polymer provides high yields and extremely high degrees of polymerization ($Pn \approx 50$). By means of adding substituents to monomers that include branching in $\gamma$-position, the solubility was improved further and higher degrees of polymerization ($Pn \approx 75$) were reached. Even though the desired material was obtained in high yield and high molecular weights, it was not possible to control defect formation completely. Every change of the monomer structure that led to high molecular weights had the opposite effect on the formation of defects, especially the formation of the exomethylene defect. These findings considered that the received materials were not pure enough and the resulting molecular weights were not high enough to test those materials for OLED applications.

Regarding the Gilch method, the performed investigations started in a different way. As already mentioned above, this synthetic procedure is a chain-growth process. Even though the Gilch method was developed already in 1960 [76], researchers were still discussing the nature of the mechanism of this reaction. While some groups regard the mechanism as anionic, others expect it to be radical [79,91–98]. Therefore, the first challenge was to identify the real nature of the Gilch mechanism. With the help of spectroscopic methods like low temperature nuclear magnetic resonance (NMR) the formation of a key compound in the polymerization process, a quinodimethane derivative (Fig. 7, intermediate **2**) was detected [99–101].

Due to this essential observation, it could be proven that the mechanism of the Gilch reaction is radical for a system that consists of the monomer, THF and potassium-*tert*-butoxide ($KO^tBu$). In case of the Gilch reaction the addition of the base leads to a quinodimethane derivative that acts as the active monomer. Afterwards, few monomers dimerize to a dimer-diradical before the further addition of the monomer leads to regular chain growth [102–104].

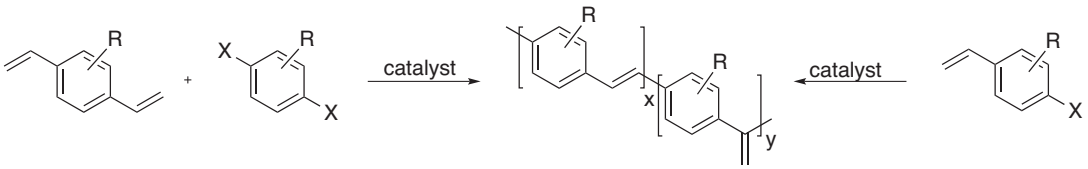


**Fig. 6.** Synthesis of PPV via the Heck methodology. X represents bromide, iodide or triflate; R is an alkyl-substituent. The catalyst system consists of a palladium-containing compound (details in the text).

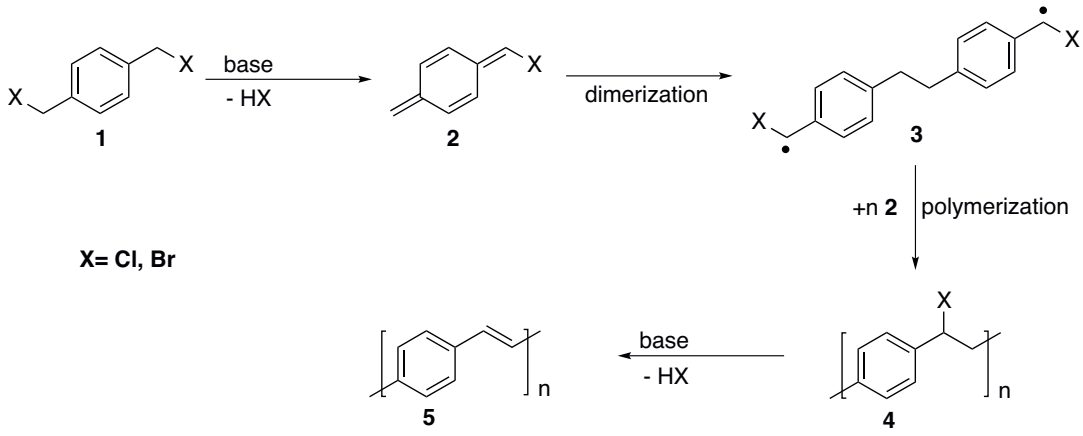


**Fig. 7.** Radical chain growth mechanism of the Gilch polymerization to PPV.

### 2.3. The tolane-bisbenzyl and the bromide defects

Given the fact that the mechanism of the Gilch reaction is radical, it is obvious where the defect formation originates from (see Fig. 8). As a radical chain growth process was observed, the addition of the monomer can take place head-to-head, head-to-tail and tail-to-tail. This mechanistic step is the origin of all defects that can be observed in Gilch-PPVs [104]. If the addition of the monomer takes place head-to-tail, it generally results in regular *trans*-configured PPV. However, sometimes the formation of *cis*-configured repeating units can be observed as well. If the addition takes place head-to-head or tail-to-tail, the formation of tolane-bisbenzyl defects (TBB) is inevitable. Imperfect dehydrohalogenation also leads to a variety of halogen defects like the vinyl-halide defect in the backbone of the polymer. The vinyl-halide defects represent the main source for long-term persistent halide in resulting Gilch-PPVs. If the addition of the monomer takes place tail-to-tail, a CHX-CHX moiety results. Here, the first dehydrohalogenation can be *trans*-selective or *cis*-selective. In case of a *trans*-selective elimination the removal of the halide proceeds very fast, whereas the *cis*-selective elimination

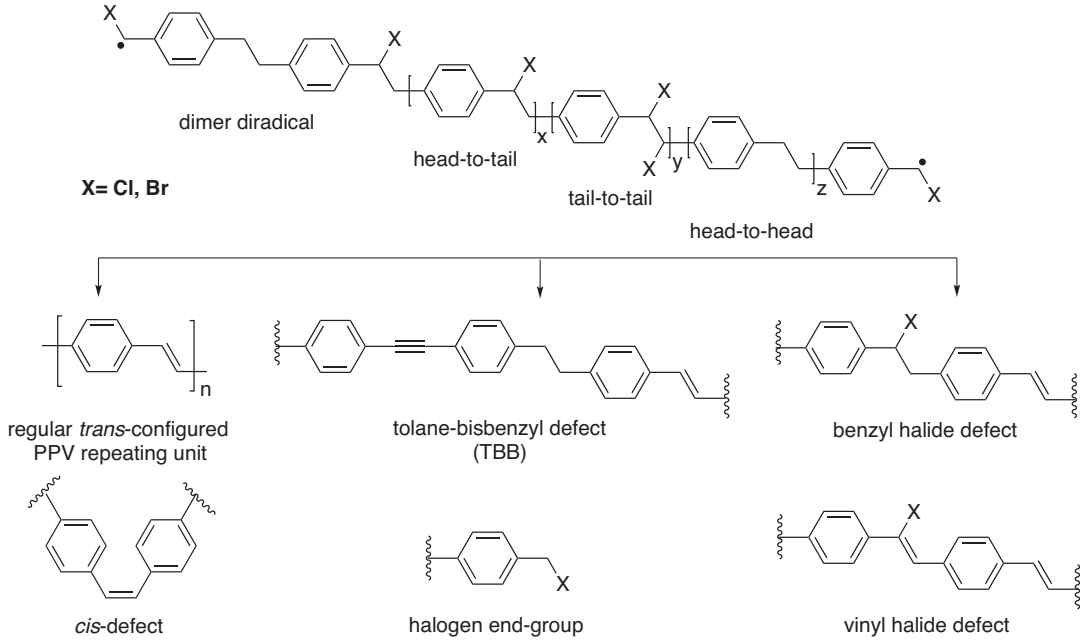


**Fig. 8.** Origin of defect formation in the Gilch synthesis of PPV. In addition to the regular *trans*-configured PPV repeating unit, possible defects in PPVs are related to *cis*-configured repeating units (*cis*-defects), imperfect dehydrohalogenation (benzyl halide defects, vinyl halide defects and halogen end groups) or the formation of correlated triple and single bonds (TBB-defects).

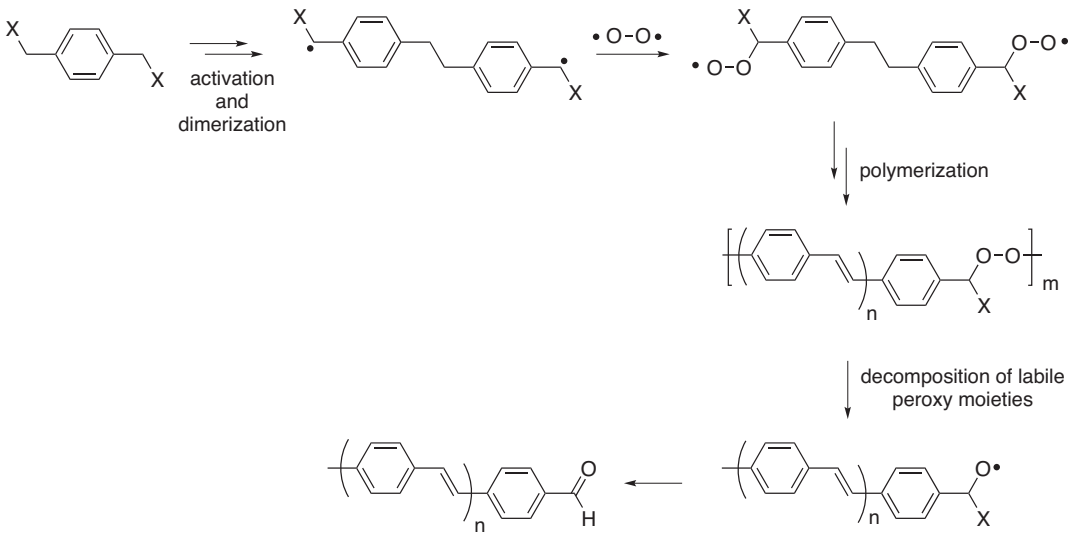


**Fig. 9.** Postulated mechanism of the Gilch polymerization when carried out in the presence of oxygen. After the initiation process and the formation of few dimerdiradical units, oxygen adds as radical to the dimerdiradical. Afterwards, regular chain growth takes place via the addition of monomer. The resulting PPV contains peroxy moieties in the polymeric backbone. Those are labile and decompose to aldehyde and carboxylic acid groups.

reaction is kinetically hindered and therefore very slow. In case the CH=CX moiety following the first dehydrohalogenation step is *trans*-configured, the second dehydrohalogenation gives triple bonds very rapidly, for the *cis*-configured counterpart it does not. This observation explains the persistence of halides in resulting PPVs.

To verify this theory the bromine content in Gilch-PPVs was monitored for reaction times between 1.5 and 96 h under otherwise constant reaction conditions. As expected from the mechanistic considerations, a decrease of the bromine content with increasing reaction times was observed. The content of bromine remaining in $OC_8C_8$-PPV amounts to 0.39 wt% (1.8% of repeating units) after 1.5 h of stirring and decreases to 0.048 wt% (0.2% of repeating units) after reaction times of 50 h [23].

For many years the TBB-defect was expected to be the limiting factor for the lifetime of OLEDs [105]. By means of our investigations this result could be refuted. As will be demonstrated later in Section 4, the most critical defects with respect to lifetime of OLEDs are not TBB-defects but all kinds of halogen defects [23]. To minimize those defects it is important to add a large amount of base and to elongate reaction times. Best results could be achieved using four equivalents of base and reaction times of about 72 h [106].

### 2.4. Preparation of different molecular weights

The proven radical mechanism of the Gilch reaction provides a means to easily modulate molecular weights of the resulting polymers. It is well known that the addition of oxygen in a radical reaction process leads to low molecular weight materials [107]. In the present case this offers the possibility to shorten the chain length during the polymerization process without effecting the vinylene double bonding like it is observed for example in the process of photooxidation [108,109]. The addition of a specific amount of oxygen shortly before the polymerization reaction is started leads to shorter PPV chain lengths.

It is assumed that the oxygen molecules add to the dimerdiradical first (see Fig. 9). Later on regular chain growth takes place. The resulting peroxy moieties in the polymeric backbone are unstable and therefore decompose rapidly under the reaction conditions. This results in polymers of lower molecular weights containing aldehyde and carboxylic acid end groups [104,109]. As will be discussed in Section 4 a high molecular weight of the polymer is important to achieve long PLED lifetimes. Consequently, the synthesis of high molecular-weight materials with a high degree of polymerization is also extremely important.

## 3. Defect engineering in oxide electrodes

Transparent conducting oxides (TCOs) serve as front electrodes in OLEDs, but also in flat panel displays and solar cells. Their fabrication as well as their electrical and optical properties are intensively studied [110–113]. In the context of organic light-emitting diodes, the TCO is used to transmit the light generated in the diode by recombination to the environment [114]. Electronically, the TCO serves as electrode for hole injection. This is quite intricate, as the commonly used TCO materials like Sn-doped $In_2O_3$ or Al-doped ZnO (AZO), are degenerately n-doped semiconductors.

The various aspects of the TCO electrode, which are relevant for operation and degradation of organic light-emitting diodes, are schematically illustrated in Fig. 10. Firstly, the electronic structure of ITO will be discussed in Section 3.1 as well as its optical and electrical properties. Understanding defect properties and the role of oxygen transport in the bulk and the vicinity of surfaces is required to finally estimate the role of oxygen exchange at the TCO surface. In Sections 3.2 and 3.3 the current understanding of bulk defect properties, including the thermodynamics of defect formation and their diffusivity, will be summarized. Surface and defect properties of ITO have both been addressed using a combination of experimental techniques like photoelectron spectroscopy and electrical conductivity measurements and computational methods like density functional theory (DFT) calculations.

For OLED operation particularly a suitable matching of energy bands is mandatory for low injection barriers, which can be adjusted by tuning the work function of the TCO layer. The polar bonding in oxides leads to a pronounced dependence of the work function on surface orientation and oxygen activity. Understanding the surface and interface properties of TCOs is therefore mandatory for optimizing the device performance. In Section 3.4 the dependence of work function of clean ITO surfaces on doping, surface orientation and surface termination will be elaborated and it will be demonstrated that commonly performed oxidizing treatments will affect only (1 0 0)-oriented surfaces.

The exchange of oxygen with the organic layer will be addressed in Section 3.5. This effect can in principle lead to fatigue of the OLED,

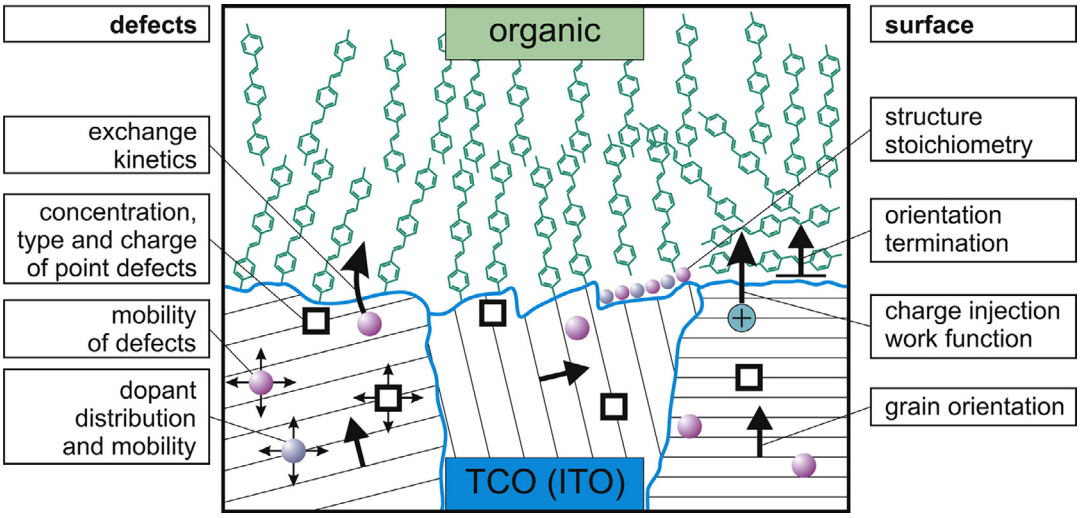


**Fig. 10.** Schematic illustration of the role of various aspects of a polycrystalline Sn-doped $In_2O_3$ (ITO) electrode in an organic light-emitting diode. The electrode serves as anode and is responsible for hole injection. This requires a large work function, which will depend on the arrangement of atoms at the surface determined by surface orientation and termination. The electrical properties of the ITO electrode are dominated by the dopants and by interstitial oxygen. The release of oxygen interstitials from the electrode may also contribute to device degradation. Thin black lines indicate orientation of crystallites. Red spheres represent oxygen, gray spheres cations, and open squares vacancies. For more details see text. (For interpretation of the references to color in this figure legend, the reader is referred to the web version of this article.)

particularly if weakly bound oxygen species are present, as e.g. oxygen interstitials in Sn-doped $In_2O_3$. However, it will be elaborated that this effect probably contributes only weakly to device degradation which might be related to the frequent use of hole injection layers like PEDOT:PSS.

### 3.1. Optical and electrical properties of ITO

The electronic structure of ITO is characterized by a valence band formed from O 2p states and a highly dispersive conduction band formed by In 5s states [115]. Although ITO has been used for decades as TCO material, the nature of its energy gap has not been understood until 2008. Thin films of ITO typically show an optical energy gap of up to 4.3 eV [116], whereas photoelectron spectroscopy reveals that the distance between Fermi level and valence band maximum, which should equal the energy gap if the Fermi energy is close to the conduction band minimum, is always less than 3.5 eV [117–119] (see also Fig. 13). Finally, Walsh et al. discovered that the optical transitions from the topmost valence band states are dipole forbidden and that strong transitions occur only from electronic states ~0.8 eV below the valence band maximum. This explains the difference between the fundamental energy gap of ~2.7 eV and the much larger optical gap of thin films. Similar behavior has actually been reported for $SnO_2$ [120]. In fact, Weiher and Ley have already reported on the absorption of $In_2O_3$ single crystals and associated the fundamental absorption edge of ~2.6 eV to a forbidden indirect transition. Although the fundamental energy gap may indeed be indirect, the smallest direct gap is only less than 100 meV larger [121]. Most recent optical absorption measurements of $In_2O_3$ single crystals also confirm a fundamental energy gap of 2.7 eV [122], although this is again assigned to an indirect transition.

The electrical properties of ITO are strongly dependent on the Sn doping level and oxygen activity during deposition [118,123]. The latter strongly influences the defect concentrations, which will be addressed in detail in Section 3.2. Highest conductivities of ITO are typically achieved with a doping level of 10 mol% $SnO_2$. Only a fraction of the dopants is active, which can be explained by their partial compensation with interstitial oxygen [123–125]. With such doping, carrier concentrations of up to $10^{21}$ $cm^{-3}$ with typical mobilities of ~40 $cm^2/V\,s$ can be achieved with polycrystalline thin films [123,124,126]. These values correspond to an electrical conductivity of ~$10^4$ S/cm. Even higher values can be obtained with epitaxial thin films grown using either pulsed laser deposition or molecular beam epitaxy on Y-stabilized zirconia single crystals [127,128].

### 3.2. Bulk defects and doping limits

In an oxide semiconductor like $In_2O_3$ the formation energy of a defect in its charge state $q$ depends on the chemical potential and the Fermi energy and is in general given by [129]:

$$\Delta G^q_{def} = G^q_{def} - G_{host} - \sum_i \mu_i n_i + qE_F \quad (1)$$

where $G^q_{def}$ and $G_{host}$ are the free energies of the material with and without the defect, respectively, $n_i$ and $\mu_i$ are the concentrations and chemical potentials of the atoms in the lattice and $E_F$ is the Fermi energy position with respect to the valence band maximum. Eq. (1) states that the defect energy is a function of the chemical potential and for charged defects also of the Fermi energy. Consequently, large variation of defect formation energy and therefore of defect concentration depending on environmental conditions and doping is possible [130–132]. Due to the crystal structure of $In_2O_3$ with its two different In-sites (called $b$ and $d$) and two different interstitial sites (called $a$ and $c$) a variety of intrinsic defects in $In_2O_3$ is possible. An extensive assessment using ab-initio density functional theory of different defect species in $In_2O_3$ including In and O vacancies and various interstitials has been published recently by Ágoston et al. [132]. The defect with the lowest formation energy under In-rich conditions is the oxygen vacancy for all reasonable values of the Fermi energy, while under oxygen rich conditions mostly oxygen interstitials are expected to be present (see Fig. 11). Indium vacancies have lowest formation energies only for Fermi levels well above the band gap.

There has been some debate of whether the oxygen vacancy is a shallow or a deep donor and whether oxygen vacancies can be the origin of the intrinsic n-type conductivity of $In_2O_3$ [131–133]. DFT calculations with hybrid functionals, which do not suffer from the underestimation of the energy gap typical for standard functionals like LDA (+U) and GGA (+U), indicate that the oxygen vacancy is a shallow donor [134].

While the origin of the intrinsic n-type nature of $In_2O_3$ is not yet fully resolved, there is common agreement that oxygen

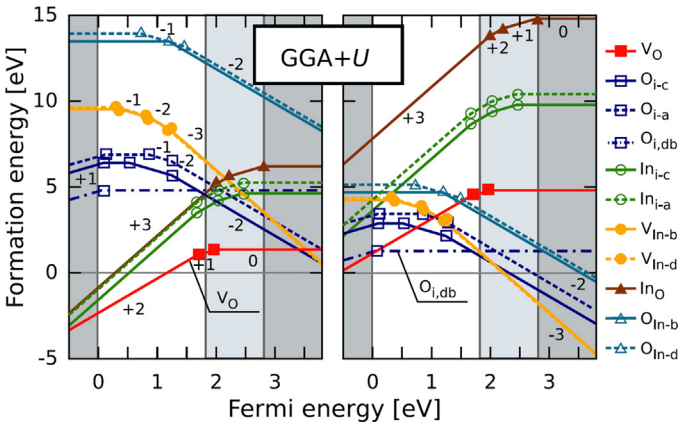


**Fig. 11.** Formation energies of intrinsic defect in $In_2O_3$ calculated using density functional theory within the GGA+U approximation [132]. The calculated energy gap is 1.81 eV. In-rich conditions (left) corresponds to $\mu(In) = 0$ eV, $\mu(O) = -(1/3)\Delta G_f(In_2O_3)$ and oxygen rich conditions (right) to $\mu(O) = 0$ eV and $\mu(In) = -(1/2)\Delta G_f(In_2O_3)$. (For interpretation of the references to color in this figure, the reader is referred to the web version of this article.)

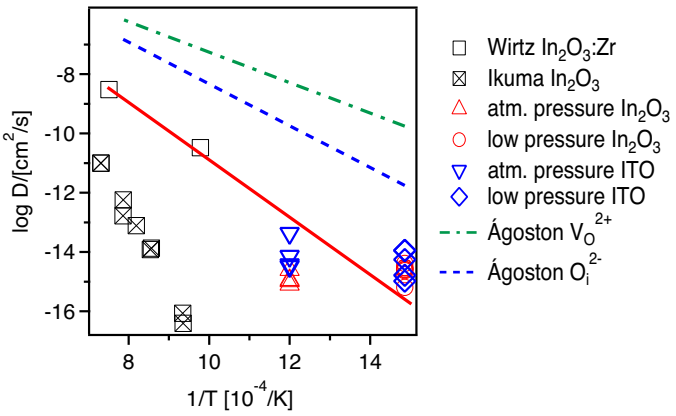


**Fig. 12.** Experimental and theoretical data on oxygen diffusion in $In_2O_3$ and ITO. Literature data are from Wirtz and Takiar [139] and from Ikuma et al. [141,142]. The diffusion coefficients calculated using density functional theory for either oxygen vacancy or oxygen interstitial diffusion are taken from Ágoston and Albe [145]. Low pressure and atmospheric pressure diffusion coefficients are extracted from conductivity relaxation measurements. The solid (red) line is a guide to the eye.

interstitials, possibly with some contribution of In vacancies, are the limiting factor for electron concentration in donor-doped $In_2O_3$ [123–125,131,135]. The limitation of carrier concentration is due to self-compensation [119,136–138], which traces back to the dependence of defect formation energies on the Fermi level position as expressed by Eq. (1) and illustrated in Fig. 11. The formation energies of (negatively charged) acceptor defects as $O_i$ and $V_{In}$ are decreasing with increasing Fermi level position[2] due to the transfer of electrons from their thermodynamic reservoir to the acceptor's energy level. Above a certain Fermi energy, the defect formation energies become negative. This is thermodynamically not possible as such a situation would correspond to more defects than possible defect sites. A material can therefore only be thermodynamically stable in the region where the defect formation energies are positive. The range of possible Fermi energies also defines the range of possible carrier concentrations. Trying to increase the electron concentration beyond the doping limit by further addition of donors will not result in an increase of carrier concentration but rather in an increase of the concentration of compensating acceptors, i.e. oxygen interstitials in the case of donor-doped $In_2O_3$. The self-compensation is also the reason why undoped $In_2O_3$ is typically oxygen deficient and donor-doped $In_2O_3$ is oxygen enriched, compared to the nominal stoichiometry.

In the next section, the diffusivity of oxygen in $In_2O_3$ and ITO will be addressed. It is important to understand if the ITO electrode can release oxygen during device operation, which can be a potential source for device degradation.

### 3.3. Oxygen diffusion in $In_2O_3$ and ITO

Due to the high concentration of interstitial sites in the bixbyite lattice (often referred to as structural vacancies), oxygen diffusion in $In_2O_3$ and ITO is often expected to be fast compared to other oxides. Experimental studies on oxygen diffusion in undoped and doped $In_2O_3$ (see Fig. 12) reveal diffusion coefficients of $D = 10^{-8}$–$10^{-15}$ cm$^2$/s at 500–1300 K [139–142]. Although these are much higher than those of many oxides, oxygen diffusion in $SnO_2$ has been reported to be even faster [143,144]. The picture of a fast oxygen diffusion due to the high concentration of interstitial sites is therefore not appropriate.

A detailed theoretical consideration of diffusion in $In_2O_3$ as performed by Ágoston and Albe [145] reveals a much more complex situation. First it needs to be mentioned that although nearest neighbor jumps of atoms with rather small migration energies as low as 0.5 eV exist, diffusion through the lattice requires multiple jumps including such with higher activation energies. The contribution of each barrier to the effective migration energy was evaluated by Ágoston and Albe using a kinetic Monte Carlo algorithm to calculate the mean-square displacement for the different types of defects. A random walk performed on the respective sublattices included all calculated microscopic barriers. As the interstitial sites contribute only to selected nearest neighbor jumps but do not provide continuous diffusion paths through the whole lattice, the effective migration energies are larger than the lowest ones and finally comparable in magnitude to activation energies of diffusion in other oxides [146,147]. According to calculated migration energies [145], the oxygen interstitial in a −1 charge state (which is only relevant for rather low Fermi energy) has the highest mobility followed by the oxygen vacancy in the +2 charge state. The oxygen dumbbell defect (index db), which corresponds to a peroxide ion on an oxygen lattice site [130] and which is dominant for oxygen diffusion in ZnO under oxygen rich conditions [146], has a slightly larger effective activation energy.

The diffusion of species can be expressed using the effective migration barriers and the concentrations of the respective defects according to

$$D = \sum_i \lambda^{eff} \cdot \Gamma^{eff} \cdot c_i \cdot \exp\left(-\frac{\Delta E_{m,i}^{eff}}{k_B T}\right) \quad (2)$$

where $\lambda^{eff}$, $\Gamma^{eff}$, $c_i$, and $\Delta E_{m,i}^{eff}$ are the effective jump distance, the effective coordination number for possible jumps, the defect concentration, and the effective migration barriers, respectively, and $i$ sums over all possible migration mechanisms (e.g. oxygen vacancy $V_O$ and oxygen interstitial $O_i$). The corresponding parameters are listed for two different temperature regimes in Table 1. The concentration of defects furthermore depends on the chemical environment and on the Fermi level position according to Eq. (1) (see also Fig. 11). Hence, the defect diffusion mechanism will change with temperature, environment and in particular with doping.

The rather low activation energy for diffusion of the In interstitial is also remarkable [145]. The temperature at which the cations should become mobile is in good agreement with an experimental observation of reversible Sn segregation for temperatures above

[2] The term *Fermi energy* is commonly used in semiconductor physics. It is actually more appropriate to use the term *electrochemical potential* of the electrons or holes.

**Table 1**
Effective migration energies $\Delta E^M_{eff}$ and effective diffusion lengths $\lambda$ for all defects in two different temperature regimes [145,148]. Additionally, the lowest energy path $\Delta E^M_{\min}$ with its corresponding jump distance $\lambda_{min}$ are given. The effective migration energy is generally higher when compared with the lowest migration energies. The last column contains the annealing temperature $T_{an}$ which indicates the temperature range in which the defect becomes significantly mobile.

| Defect | $q$ | $\Delta E^M_{eff}$ [eV] | $\lambda_{eff}$ [Å] | $\Delta E^M_{eff}$ [eV] | $\lambda_{eff}$ [Å] | $\Delta E^M_{\min}$ [eV] | $\lambda_{min}$ [Å] | $T_{an}$ [K] |
|---|---|---|---|---|---|---|---|---|
| | | 1500 K–1700 K | | 700 K–900 K | | | | |
| $V_O$ | 0 | 1.83 | 3.49 | 1.77 | 2.44 | 1.53 | 2.94 | 640 |
| | +1 | 1.20 | 3.58 | 1.13 | 2.39 | 0.77 | 2.94 | 410 |
| | +2 | 1.10 | 3.32 | 1.02 | 2.26 | 0.71 | 2.94 | 370 |
| $V_{In}$ | −3 | 2.26 | 4.09 | 2.27 | 4.24 | 2.21 | 3.83 | 820 |
| | −2 | 2.21 | 4.13 | 2.17 | 3.35 | 2.11 | 3.83 | 800 |
| $O_i$ | −2 | 1.41 | 6.36 | 1.40 | 5.96 | 1.22 | 3.62 | 480 |
| | −1 | 0.74 | 3.94 | 0.77 | 4.62 | 0.52 | 3.62 | 270 |
| $O_{db}$ | 0 | 1.19 | 2.52 | 1.20 | 2.65 | 1.00 | 2.52 | 430 |
| $In_i$ | +3 | 1.67 | 7.27 | 1.66 | 7.08 | 0.42 | 2.14 | 580 |
| | +2 | 1.44 | 5.99 | 1.39 | 4.41 | 0.29 | 2.14 | 500 |

~300 °C [118]. Mobility of cations does also seem to be necessary to explain time dependent changes of carrier mobility and concentration of ITO at elevated temperatures [149]. That cations are mobile at comparatively low substrate temperatures is also predicted by the effective diffusion parameters for interstitial In in Table 1. Segregation of Sn dopants, which are expected to show similar diffusivity as In host atoms, has also been observed at ITO surfaces. Reversible changes of the Sn surface concentrations have been found in response to a change of the oxygen activity at temperatures $\gtrsim$300 °C [118].

### 3.4. Work function of Sn-doped $In_2O_3$ and other transparent oxide electrode materials

The energy band alignment at interfaces with organic semiconductors is, to a large extent, described by alignment of the vacuum levels at the interface [33,150–152]. A small barrier for hole injection is therefore obtained by increasing the work function of oxide electrode. Historically, the most widely used oxide electrode is ITO, which still shows the highest conductivities among the standard TCO materials. Another advantage of ITO compared to other TCOs is the easy structuring of the electrode by a chemical etching process. The etchability of ITO is in between ZnO and $SnO_2$, which are etching either too fast or too slow.

Numerous studies have been devoted to the manipulation of the work function of ITO. A complete review of the various treatments and the resulting work functions is beyond the scope of this article. Highly oxidizing treatments as UV-ozone or oxygen plasma treatments have been found to significantly increase the work function [153–157] and became a standard for electrode treatment before deposition of the organic semiconductors. In most of the studies the details of the oxide's surface structures have not been considered. First of all, it should be mentioned that the work function $\phi$, which is determined by the energy difference between the vacuum level and the Fermi energy ($\phi = E_{vac} - E_F$), is affected by the variation of two independent properties (see Fig. 13): (i) the position of the Fermi level with respect to the band edges ($E_F - E_{VB}$), which is determined by the bulk doping and (potential) surface band bending. Band bending at a surface can be induced by various sample treatments, but is typically not present at in-situ prepared samples [119]; (ii) the ionization potential $I_P$, which is the position of the vacuum energy with respect to the band edges ($I_P = E_{vac} - E_{VB}$). A variation of the surface dipole of a material leaves the Fermi level position unaffected but changes the ionization potential. In general, an oxygen-rich surface termination results in a larger ionization potential. One therefore has to expect that the ionization potential, and consequently also the work function, depends on the oxygen activity.

The oxygen activity during preparation of the TCO electrode also affects its bulk doping via a change of defect concentration and therefore the Fermi level position with respect to the band edges [119]. It is therefore important to determine both quantities, Fermi level position and work function, simultaneously. This is possible using photoelectron spectroscopy. Comprehensive studies of Fermi level positions and work function in dependence on doping and oxygen activity using in-situ sample preparation by magnetron sputtering have been performed for ZnO, $SnO_2$ and $In_2O_3$ [119,158,159]. The results are summarized in Fig. 13. The relevant work functions are those obtained for the highest doping levels, i.e. for the highest possible Fermi energies. The corresponding work functions for $SnO_2$ and $In_2O_3$ at the highest doping level are comparable with values around 4.7–4.8 eV, while significantly lower work functions are obtained for ZnO.

The variation of the ionization potential, which corresponds to the variation of work function at a given Fermi energy, can be rationalized by the dependence on surface orientation and termination [119,158,159]. For ZnO, a low ionization potential is obtained for the Zn-terminated (0 0 0 1) surface orientation, while higher $I_P$ are obtained for other surface orientations [160]. For $SnO_2$, the variation of ionization is related to different surface terminations, which are largely related to the two different oxidation states of Sn [161,162]. This variation has been observed for all low index surfaces of $SnO_2$ [163].

The situation for $In_2O_3$ surfaces is different as both surface orientation and termination contribute to the variation of ionization potentials. First of all, the electrostatic stability of the

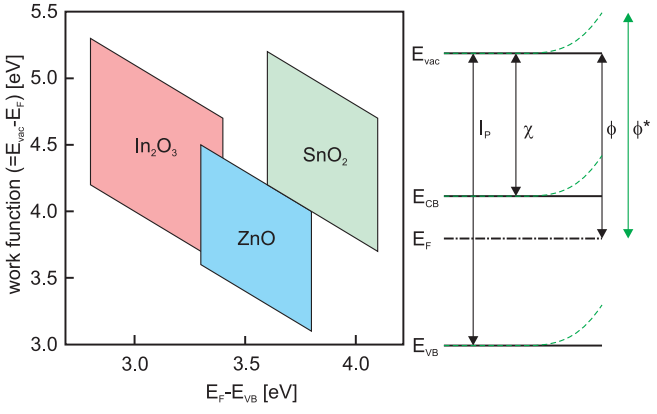


**Fig. 13.** Schematic range of Fermi level positions and work functions of highly doped polycrystalline ZnO, $SnO_2$ and $In_2O_3$ as obtained from ultraviolet photoelectron spectroscopy (after [159]). The lower bounds of the Fermi level positions correspond to the energy position of the conduction band minimum and the upper bounds to the highest possible band filling observed. The right part shows the energetic situation at a surface with (dashed lines) and without surface band bending (solid lines) and the definition of the work function $\phi$, the ionization potential $I_P$, and the electron affinity $\chi$. The work function in the presence of surface band bending is denoted by $\phi^*$.

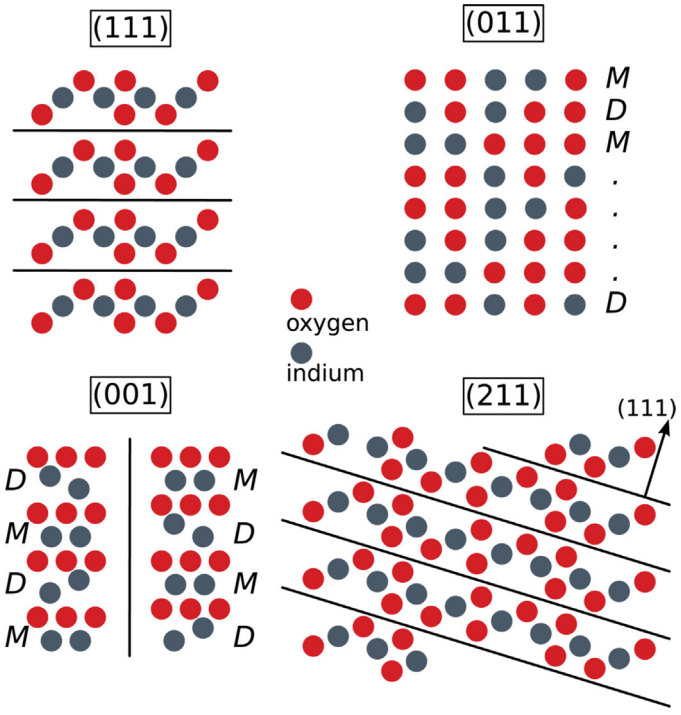


**Fig. 14.** Schematic cross-sections of low-index $In_2O_3$ surface structures [166] (copyright: The American Physical Society).

various surface orientations have to be considered [164]. A potential surface instability is caused along polar directions, i.e. along a direction where negatively and positively charged atomic planes are arranged to form a permanent dipole moment. The various polarities can be classified according to a scheme outlined by Tasker [165]. This is schematically illustrated for the low-index surfaces of $In_2O_3$ in Fig. 14.

According to Tasker's classification, the $In_2O_3$(1 1 0) surface is Tasker type I, which is non-polar. The $In_2O_3$ (1 1 1) surface is a Tasker type II surface, as dipole-free O-In-O planes can be stacked along the (1 1 1) direction. The $In_2O_3$ (1 0 0) surface is a polar, Tasker type-III surface, where the electric dipole moments of the stacked In–O planes have to be compensated by surface charges or surface reconstructions in order to avoid the so-called polar catastrophe. Consequently, it has to be expected that the (1 1 0) and (1 1 1) surfaces are more stable than the (1 0 0) surface and that significant surface reconstructions do only occur for the latter. This is in good agreement with calculations of surface reconstructions [166,167].

The thermodynamic stability of the various surface terminations as extracted from [166] is given in Fig. 15. For most values of the chemical potential, the (1 1 1) surface orientation is the most stable. Only at very low oxygen chemical potentials, the (1 0 0) surface termination becomes more stable. These calculations are in line with observations of flat epitaxial film growth under In-rich growth conditions using molecular beam epitaxy [168]. During magnetron sputter deposition of $In_2O_3$ films, flat (1 0 0) oriented films are also observed under very oxygen-rich conditions [169]. According to the thermodynamic data in Fig. 15, this requires a positive oxygen chemical potential, which would correspond to an effective oxygen pressure >1 bar. This is not unreasonable, as the addition of oxygen to the sputter gas results in implantation of oxygen into the growing film [170,171].

Experimentally determined ionization potentials of $In_2O_3$ and ITO films vary between ~7 and ~8.1 eV [117,118,158,172]. With the help of measurements of epitaxial films (see Fig. 16b), the lower

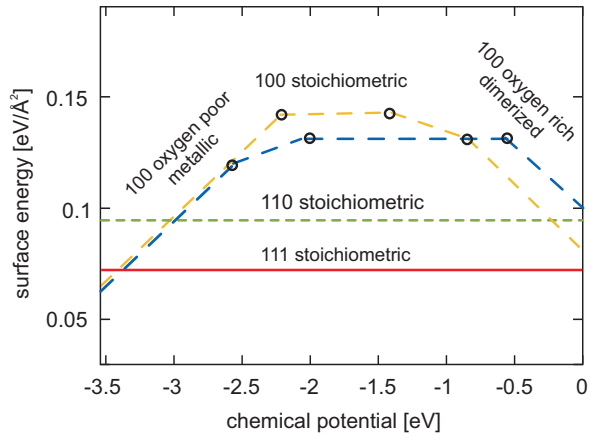


**Fig. 15.** Surface energies of different $In_2O_3$ surfaces in dependence on oxygen chemical potential as extracted from [166].

boundary can be attributed to the (1 1 1) surface orientation, which is in good agreement with the DFT calculations (see Fig. 16a).

For epitaxial films with (1 0 0) surface orientation, the ionization potential is found to be 7.7 eV. The ionization potentials of epitaxial films agree with those obtained from polycrystalline films with strongly preferred (2 2 2) or (4 0 0) orientation [119]. It seems therefore reasonable to associate the ionization potential of ~7.7 eV,

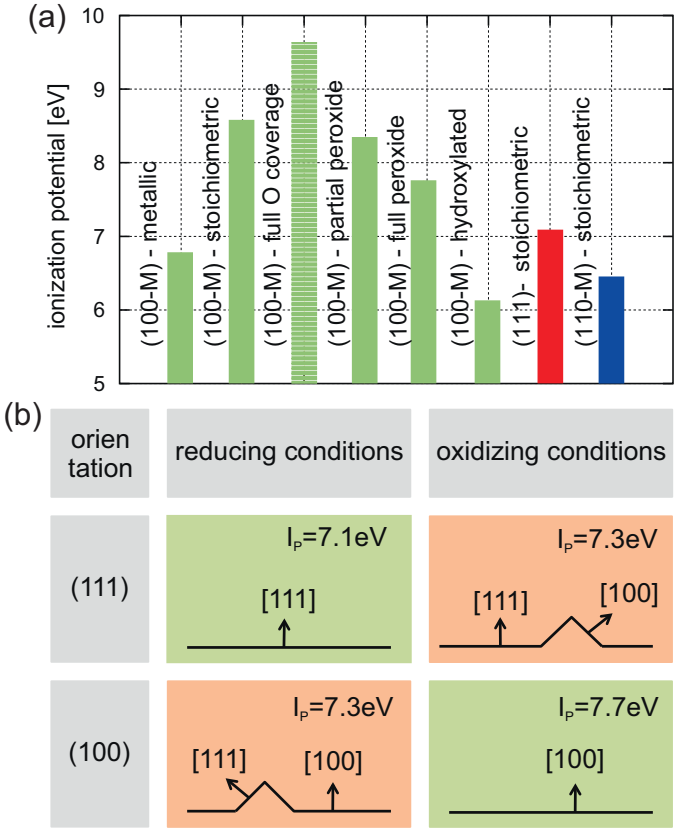


**Fig. 16.** (a) Ionization potentials of various $In_2O_3$ surfaces calculated using density functional theory [169]. (b) Ionization potentials measured using photoelectron spectroscopy at surfaces of epitaxial $In_2O_3$ films [169]. For sputter deposited films, flat (1 1 1) surfaces form under more reducing deposition conditions, i.e. by using pure Ar as sputter gas, while flat (1 0 0) surfaces form under oxidizing deposition conditions, i.e. with the addition of oxygen to the sputter gas. For these conditions, the ionization potentials measured by UPS are in good agreement with theory. Deposition under oxidizing conditions onto (1 1 1)-oriented substrates or under reducing conditions onto (1 0 0)-oriented substrates result in facetted surfaces with intermediate ionization potentials.

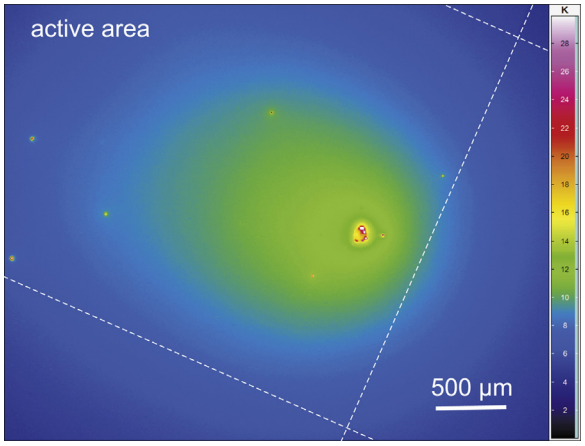


**Fig. 17.** Thermogram of a PLED operated at a constant current density of 50 mA/cm$^2$ exhibiting several hot spots. The active area is marked and has a size of 10 mm$^2$. The temperature is given relatively to the temperature of the undriven device (room temperature). The PLED has been operated for several 100 h and is beyond its $t_{50}$ lifetime. Due to the high temperatures occurring at the hot spots, the device died by a sudden death shortly after the thermogram has been taken. (The reader is directed to the web version of this article to view this picture in color.)

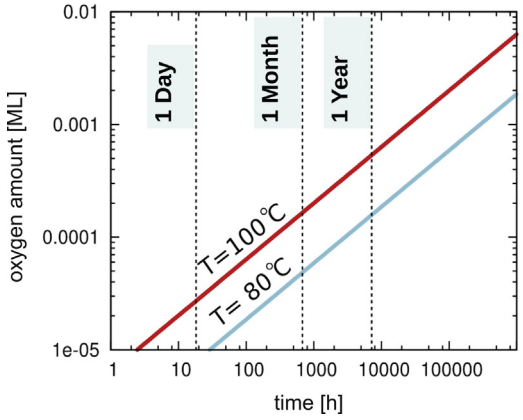


**Fig. 18.** Amount of oxygen expressed in monolayers (ML) released from ITO as a function of time, calculated using computationally derived diffusion coefficients.

which is the value typically measured at surfaces of polycrystalline ITO films [117,118,158], to a (1 0 0)-oriented surface. It is suggested by the DFT calculations (Fig. 16a) that this value corresponds to a full peroxide ($O_2^{2-}$) surface termination. But this termination is only stable for pure $In_2O_3$ and not for ITO, as the oxygen dimers at the surface should dissociate at high Fermi level position [166].

With the knowledge about the surface properties, some important consequences for the behavior of ITO in OLEDs can be inferred. First of all, one has to expect that the ionization potential and the work function are not homogeneous at the interface due to the polycrystalline nature of ITO. In particular, high work functions and therefore low injection barriers for holes are only expected for (1 0 0)-oriented surfaces. Charge injection is therefore expected to be spatially inhomogeneous, which can lead to locally enhanced currents, a possible origin of device failure [173]. Due to a locally enhanced current (and a simultaneously locally increased light emission) the temperature of the OLED is locally increased as well. Fig. 17 illustrates exemplarily a PLED exhibiting hot spots that developed during a fatigue experiment close to the catastrophic failure of the device.

The inhomogeneous charge injection is expected to become more pronounced upon the typical oxygen plasma or UV ozone treatments. According to the surface phase diagram depicted in Fig. 15, the (1 1 0) and (1 1 1) surface terminations are not expected to depend on oxygen activity. Such changes are only expected for the (1 0 0) surface orientation, where a higher oxygen chemical potential should lead to an increase of oxygen at the surface. Consequently, the ionization potential, and hence the work function, will only change upon oxidation/reduction for (1 0 0)-oriented parts of the surface. The magnitude of the changes can be quite large as indicated by the ionization potentials for the different surface orientations and terminations (see Fig. 16b), which are obtained from density functional theory calculations [148,169].

Avoiding inhomogeneous charge injection can be one of the reasons, why amorphous transparent conductors like $In_2O_3$-ZnO (IZO) are also suitable as transparent electrodes [174,175]. The ionization potentials of IZO films are also found to be ~7.7 eV, resulting in work functions of 4.5–5 eV, depending on the Fermi level position [176]. A homogenization of charge injection may also be a beneficial effect of non-crystalline buffer layers like $MoO_3$, $WO_3$, or PEDOT:PSS [177–180].

### 3.5. Oxygen exchange at ITO surfaces and ITO/organic interfaces

A final aspect of the transparent oxide electrode is the exchange of oxygen at the interface with the organic materials. Such an effect has been observed during deposition of Zn-phthalocyanine (ZnPc) onto ITO samples, which were prepared with addition of oxygen and therefore exhibit a high oxygen interstitial concentration [117]. The release of oxygen during deposition of the organic molecules was evident from X-ray photoelectron spectroscopy measurements by the observation of an increase of carrier concentration at the ITO surface and also by the observation of chemical oxidation products.

Oxygen exchange at surfaces is typically governed by the kinetics of the surface reactions [181,182], which is very often prohibiting defect equilibria, in particular at lower temperature [183,184]. It is therefore quite remarkable, that removal of oxygen from ITO during deposition of organic molecules is observed even at room temperature [117]. Together with oxygen diffusion, the exchange of oxygen is a precondition to establish equilibrium defect concentrations. As the defect concentrations are affecting the carrier concentrations in an oxide, conductivity relaxation experiments, i.e. the measurement of the temporal evolution of electrical conductivity as a function of temperature and oxygen pressure, are suitable for accessing oxygen exchange. Using such measurements, noticeable changes of conductivity in response to a change of oxygen content in the atmosphere are only observed for temperatures >200 °C [149]. These temperatures are in good agreement with the calculated equilibration time limited by oxygen diffusion using Eq. (2). This furthermore demonstrates that the change of oxygen interstitial concentration, which is the origin of conductivity changes for $T > 200$ °C is limited by oxygen diffusion in the film and not by surface oxygen exchange.

With the calculated oxygen diffusion coefficients [145], it is possible to determine how much oxygen will be extracted from ITO in the diffusion limited regime. The results derived for $T = 80$ °C and 100 °C are shown in Fig. 18. At 100 °C, e.g. only $5 \times 10^{-4}$ monolayers of oxygen can be extracted from ITO in one year. This can hardly be considered as a considerable contribution to degradation of organic molecules in an OLED device. The calculation does, however, not take the electric field into account, which will partially penetrate the ITO electrode due to its low carrier concentration, compared to a metal electrode [185]. The amount of oxygen released from ITO may also be sufficient to induce a modification of the interface, resulting, e.g. in a change of injection barrier.

Oxygen exchange at ITO surfaces may be suppressed by suitable surface coatings. Using $Al_2O_3$ for this purpose seems a reasonable choice, as oxygen diffusion is rather slow in $Al_2O_3$. Furthermore, a monolayer of $Al_2O_3$ can enhance the work function

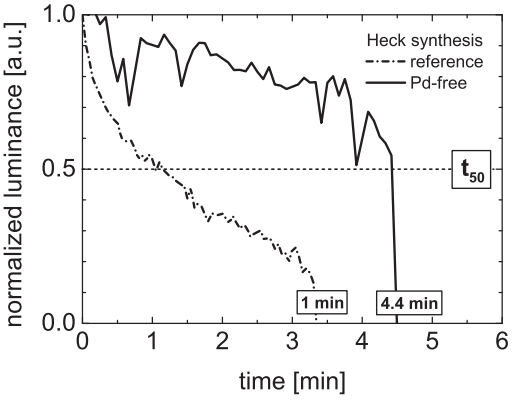


**Fig. 19.** Effect of catalyst residues and low polymerization degree from Heck synthesis on the temporal luminance evolution of $OC_6C_6$-PPV PLEDs driven at 50 mA/cm$^2$. The device structure was: ITO/PEDOT:PSS/$OC_6C_6$-PPV/Ca/Al.

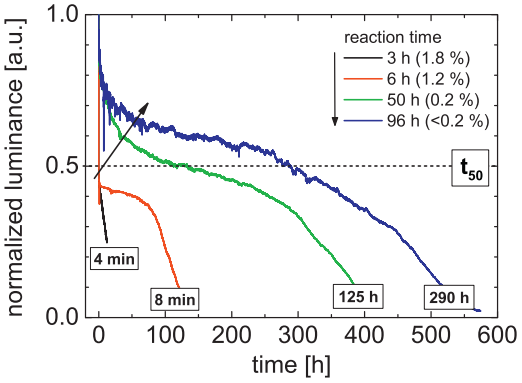


**Fig. 20.** Influence of the reaction time of $OC_8C_8$-PPV during Gilch synthesis on the luminance evolution and the lifetime of PLEDs driven at a constant current density of 50 mA/cm$^2$. The percentage of the PPV-repetition units bearing the bromine defect is included in brackets for the respective reaction times. The device structure was: ITO/PEDOT:PSS/$OC_8C_8$-PPV/Ca/Al.

considerably [170], which may reduce the injection barrier for holes. $Al_2O_3$ has also been tested as a buffer layer in OLEDs [186]. The effect of $Al_2O_3$ deposition onto ITO depends very much on the deposition technique. During reactive magnetron sputtering, oxygen ions are accelerated toward the substrate and implanted into ITO, which leads to a surface depletion of electrons [170]. In contrast, atomic layer deposition (ALD) leads to the extraction of interstitial oxygen and to a surface accumulation of electrons [187]. The characteristic self-limited growth in ALD is therefore disabled due to ITO acting as oxygen source. The suppression of oxygen exchange by deposition of 0.5 nm of $Al_2O_3$ layer is stronger for sputtered $Al_2O_3$ films, which has been related to a better morphology. However, no improvement in device stability has been observed with the use of $Al_2O_3$ buffer layers at the anode. This might give indications that the effect of oxygen diffusion on fatigue is minor or that it is camouflaged by other dominating effects.

## 4. Influence of defects on transport properties and lifetime

### 4.1. Device operation in defect-enriched systems

For PPV polymers prepared by the Gilch route, several constitutional defects of the PPV-chain have been identified as displayed in Fig. 8, affecting up to several percent of the repetition units (see Fig. 20). It has been believed for a long time that especially the TBB-defect plays a major role for the degradation of PPV-based devices [105]. However, it was demonstrated that the previously often overlooked effect of an incomplete dehydrohalogenation of the PPV-intermediates during the synthesis leads to partially non-conjugated polymer chains with remaining halogen in the backbone resulting in a drastically decreased performance and lifetime of the PLEDs [23]. Bromine containing precursors have been used for the polymer synthesis, therefore vinyl bromide defects are considered. The PPV derivative under investigation is $OC_8C_8$-PPV.

#### 4.1.1. Lifetime evolution

For practical applications of PPV-derivatives, the choice of the Heck route for materials synthesis is unfavorable. As will be shown Heck-PPVs suffer from residual metal catalysts limiting their lifetime. As mentioned in Section 2.2 a palladium-containing catalyst system was used for the synthesis. Parts of this compound remain in the final polymer and acts as quenching centers [188,189]. For poly[2,5-bis(hexyloxy)-1,4-phenylene-vinylene] ($OC_6C_6$-PPV) it was show exemplarily that the lifetime of the respective PLEDs can be increased if the metal catalyst content is reduced (see Fig. 19). Despite this fact, it is obvious that the obtained lifetimes in both the Pd-depleted and the Pd-rich devices are much too short, just a few minutes. This finding is attributed to the low molecular weights of the PPVs synthesized via the Heck route yielding an insufficient entanglement of the polymer chains. As will be shown later a high molecular weight of about $10^5$ g/mol or beyond is needed in order to produce long-lived PLEDs. In addition, these devices seem to suffer from sudden death, i.e. an unexpected and complete emission loss, more often than Gilch synthesized PPVs. In the two examples shown in Fig. 19, the light emission stops as already discussed in Section 1.2 and the voltage drops to around 2 V.

For the Gilch synthesis the dehydrohalogenation step is decisive for the performance of the device as well as its lifetime. A short reaction time is equivalent to a high amount of bromine residue in the PPV polymer (see values given in Fig. 20), yielding low currents and luminance values for the final devices [23] as well as short lifetimes below one hour as indicated by the temporal evolution of the luminance in Fig. 20 recorded for a PLED operated at a constant current density of 50 mA/cm$^2$. In addition, bromide defect enriched devices (reaction time of 3 h and 6 h) suffer from a dramatic initial drop of the luminance to about 40% of the initial luminance within the first 30 min of the measurement, whereas the luminance only drops to 85–90% for the devices with lower bromine contents. The lifetimes extracted from Fig. 20 are considerably increased for bromine contents well below 1%, meaning that less than 1% of repetition units bear the defect. The 96 h reaction time yields a purity of the material beyond the detection limits of ion chromatography and elemental analysis used to measure the bromine content [23].

#### 4.1.2. Mobility evolution and transport phenomena

Even though the performance and the lifetime of the PLEDs are influenced distinctly by the amount of bromide defects, it has been found that the hole mobility is not affected. As PPV derivatives are hole-dominated materials [190,191] the mobility of holes has been measured by the time-of-flight (TOF) method. Fig. 21 depicts exemplary TOF current transients recorded for devices with halogen defect-enriched (3 h reaction time) and halogen defect-poor (96 h reaction time) PPV-layers. Both curves are examples for a non-dispersive transport where a current plateau appears followed by a kink at the transit time of the drifting charges [192,193]. It is obvious that the shapes of the transients are very similar, resulting in similar transit times for holes and consequently in similar hole mobilities in the range of $1 \times 10^{-4}$ cm$^2$V$^{-1}$s$^{-1}$. In addition, independently on the bromide defect content only a slight field dependence of the mobility is observed [23].

Even though the electron transport in PPVs is limited by strong trapping [194–196] and electron-only devices made of

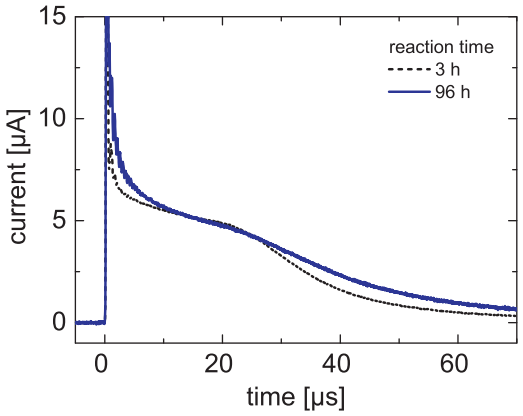


**Fig. 21.** Measured TOF current transients for PLEDs with $OC_8C_8$-PPV synthesized with short (3 h) and long (96 h) reaction time during Gilch synthesis. The currents of the 96 h material have been scaled by a factor of 10 to allow for a better comparison of the curve shapes. The device structure was: Al/$OC_8C_8$-PPV/Al. Photoexcitation was obtained by laser irradiation at 532 nm.

halogen defect-poor PPV indicate a slightly increased electron mobility for the lowest bromine content, the formation of electron traps by bromine cannot explain the inferior device performance of bromide defect-enriched bipolar PLEDs since the device performance is not only determined by the charge carrier transport but also by charge carrier injection. Consequently, the electrodes might predominantly determine the variation in the current–voltage-characteristics upon changed reaction time. Indeed, strong indications have been found by secondary ion mass spectroscopy (SIMS) measurements showing a segregation of the available bromine residue at the anode side as depicted in Fig. 22 for an electrically fatigued PLED. This yields undesired reaction products at the interface between the organic semiconductor and the anode, thereby affecting hole injection. As will be discussed in the next paragraph a chemical reaction between bromine and the electrode is also assumed at the cathode side, thereby affecting electron injection as well.

In order to explain how residual bromine affects freshly prepared and electrically fatigued devices, the following model has been developed [23]: Due to the well-matched work function of the calcium cathode to the LUMO level of PPV, electrons will diffuse into the fresh device to establish thermodynamic equilibrium. Yet, the developing back-driving electric field prevents a deep penetration of the electrons into the polymer, thereby confining the formed negative charge carrier reservoir to a region close to the cathode. Bromide defects located in this region can capture an electron from the reservoir yielding bromine anions. These negatively

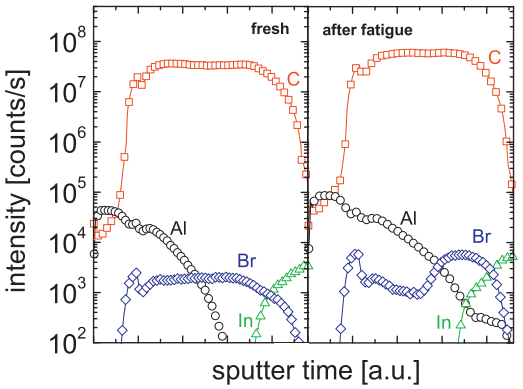


**Fig. 22.** SIMS profiles of a fresh and an electrically fatigued PLED sputtered from the top electrode side with $Cs^+$-ions. The device structure was: ITO/$OC_8C_8$-PPV/Ca/Al.

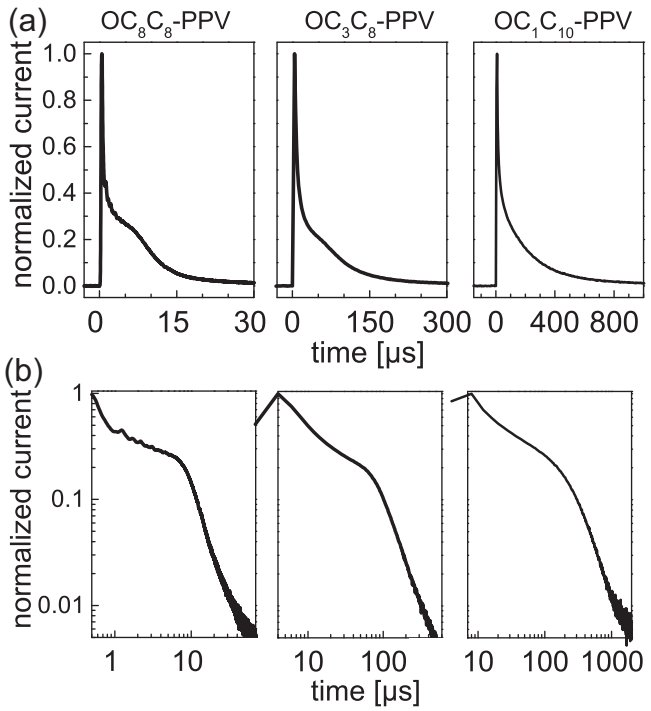


**Fig. 23.** TOF current transients for three PPV-derivatives with different side chain symmetry measured at reverse bias of 40 V in linear (a) and double logarithmic representation (b). The device structure was: ITO/PEDOT:PSS/PPV/Ca/Al. Photoexcitation was obtained by laser irradiation at 532 nm.

charged ions can drift in the build-in field and especially in the enhanced field of the space charge regime to the cathode and react there forming a calcium salt. As a result the injection properties of the cathode will be deteriorated, leading to an inferior performance of bromide defect-enriched fresh devices. Experimental evidence for this mechanism comes from the finding that the performance of electrically fatigued devices can be partially restored after the wet-chemical removal of the cathode and subsequent evaporation of a new one onto the fatigued layer stack.

The influence of bromide defects can be understood in a similar way for electrically fatigued devices. As the fatigue is performed using a certain forward current constantly applied to the diode, electrons and holes are injected and transported into the polymer. Now, bromide defects located in the bulk can also capture electrons to form bromine anions. Those drift in the forward bias field toward the anode where again a metal salt forming reaction with indium takes place [37].

### 4.2. Device operation in halogen defect-poor systems

After having identified the importance of the bromide defect for the PLED performance and lifetime, subsequent investigations on the transport properties of different PPV derivatives and on further factors that influence device stability have been conducted using Gilch-synthesized PPVs all with low bromide defect concentrations.

#### 4.2.1. Effect of the side chain symmetry on transport phenomena and fatigue

Besides $OC_8C_8$-PPV with symmetric side chains, $OC_3C_8$-PPV with increasing side chain asymmetry and the commonly known derivative $OC_1C_{10}$-PPV or MDMO-PPV with the most asymmetric side chain geometry have been investigated. While the lifetimes of the respective PLEDs are similar (several 100 h) their transport properties differ distinctly.

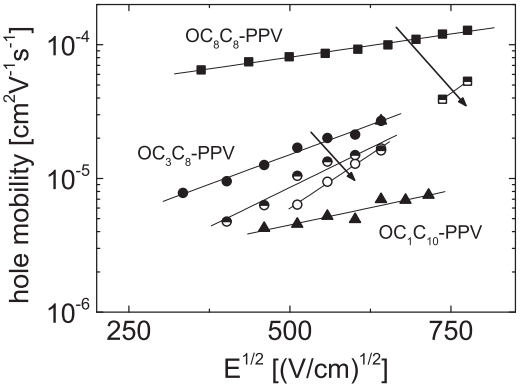


**Fig. 24.** Hole mobility of three PPV-derivatives as a function of the applied electric field calculated from TOF transients for fresh (filled symbols) and electrically fatigued (half-filled and open symbols) PLEDs. The $OC_3C_8$-PPV devices have been fatigued in two steps.

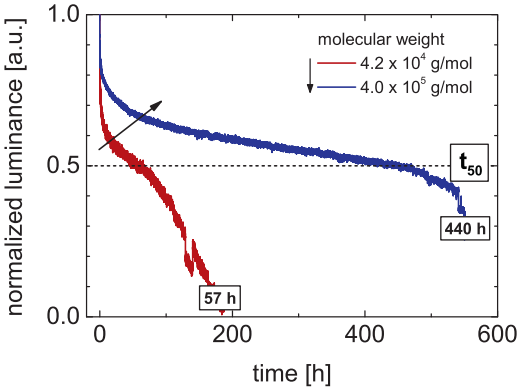


**Fig. 25.** Evolution of the luminance and lifetime of $OC_3C_8$-PPV PLEDs with different molecular weights during electrical fatigue at a constant current density of 50 mA/cm². The device structure was: ITO/PEDOT:PSS/$OC_3C_8$-PPV/Ca/Al.

Fig. 23 illustrates TOF current transients measured for devices with the three PPV derivatives in linear and logarithmic scale. It is evident that the curves change with the asymmetry of the side chains: While the TOF curves for $OC_8C_8$- and $OC_3C_8$-PPV-based devices display a plateau-like shape indicative for non-dispersive transport [197], the transients for the $OC_1C_{10}$-PPV devices show a featureless decay indicating dispersive charge carrier transport [197,198]. Nevertheless, replotting the current transients for $OC_1C_{10}$-PPV devices using double logarithmic axes yields a kink (see Fig. 23b). Taking this time as transit time allows for the calculation of the hole mobility. It should be noticed that this value is no material parameter any more but characteristic for the device geometry, e.g. the layer thickness used. Consequently, an increasing asymmetry of the side chains yields a transition from non-dispersive to dispersive hole transport.

As the transit times of the asymmetric side chain polymers $OC_3C_8$-PPV and $OC_1C_{10}$-PPV shift to higher values compared to $OC_8C_8$-PPV, the hole mobilities will decrease with increasing asymmetry of the side chains. Fig. 24 depicts the calculated hole mobilities as a function of the applied electric field: The symmetric side chain derivative $OC_8C_8$-PPV has the highest mobility on the order of $10^{-4}$ cm$^2$ V$^{-1}$ s$^{-1}$ while the derivative with the most asymmetric side chain, $OC_1C_{10}$-PPV, exhibits the lowest hole mobility of about $5 \times 10^{-6}$ cm$^2$ V$^{-1}$ s$^{-1}$. This is related to the decreased conformational freedom of polymer chains with symmetric side chains as described by Martens [199] and to the better molecular ordering in the solid resulting in a decreased energetic disorder thereby facilitating charge carrier transport between the polymer chains. These findings are in agreement with previous results from literature [199,200].

Repeating the TOF measurements with electrically fatigued devices allows for the determination of the hole mobility change due to the fatigue. As indicated in Fig. 24 the hole mobilities of all PPV-derivatives decrease more and more with prolonged electrical fatigue. In addition, the hole transport gets more dispersive for all derivatives [22]. In the case of $OC_1C_{10}$-PPV, which already displayed dispersive transport before the fatiguing, the transit time could not be obtained any more for fatigued devices, not even from the double logarithmic current plots. Consequently, mobilities could not be calculated. The lines included in Fig. 24 are fits according to the Poole–Frenkel-like field dependence of charge mobility at a constant temperature $\mu = \mu_0 \cdot \exp(\gamma\sqrt{F})$ with a zero field mobility $\mu_0$, a field factor $\gamma$ and the electric field $F$ [199,201]. Obviously, the field dependence changes with increasing fatigue level, i.e. increasing operation time, as illustrated for $OC_3C_8$-PPV. According to Martens and coworkers this can be related to an increasing energetic disorder of the polymer [199], that is here induced by fatigue. The detailed fitting parameters are given in Ref. [22].

#### 4.2.2. Effect of the molecular weight on the lifetime

Not only a low defect content but also a high molecular weight of the semiconducting polymer is important for a high efficiency and a long device lifetime. Adding oxygen shortly before the Gilch polymerization is started as described in Section 2.4 allows for the controlled shortening of the polymer chains and the preparation of polymers with two different molecular weights. Preparing two sets of samples with $OC_3C_8$-PPV of high ($4.0 \times 10^5$ g/mol) and lower ($4.2 \times 10^4$ g/mol) molecular weight it could be shown that the device performances as well as the lifetimes differ distinctly. Fig. 25 depicts the results of the respective fatigue experiment. By increasing the molecular weight of the PPV derivative by one order of magnitude, the lifetime is also increased by a factor of nearly 8. Thereby, it was demonstrated that the chemical synthesis of the functional polymers should also aim at producing high molecular weight materials of $10^5$ g/mol or higher. The reasons for the better performing high-molecular weight materials are likely related to the lower density of end-chains and to better film forming properties.

#### 4.2.3. Factors influencing electrical fatigue

In the previous sections the influences of bipolar electrical operation on the lifetime and transport properties of PLEDs based on specific, chemically modified PPVs have been already discussed. Yet, due to the aforementioned complex function of OLEDs that also holds true for single layer fluorescent devices it is not easy to assign which process actually is responsible for the observed fatigue behavior. In the case of PPV-based PLEDs one might argue that due to the hole-dominance in the devices the thus flowing hole currents that traverse almost the complete layer thickness before they find electrons to recombine with may play a major role for the fatigue. However, it could be demonstrated that the transport properties in hole-only diodes with PEDOT:PSS and Au electrodes are not changed due to electrical fatigue. According to Fig. 26A the TOF current transients measured before and after electrical fatigue are identical, pointing to invariance of the hole mobility. In spite of this, the calculation of the hole mobility has been abandoned for the present device structure due to the very high injection currents and the consequently undefined charge carrier distribution in the PPV layer.

Unlike in usual TOF experiments a reverse bias situation, i.e. a suppression of charge carrier injection, cannot be obtained in the case of ITO/PEDOT:PSS/$OC_8C_8$-PPV/Au devices. Exchanging both

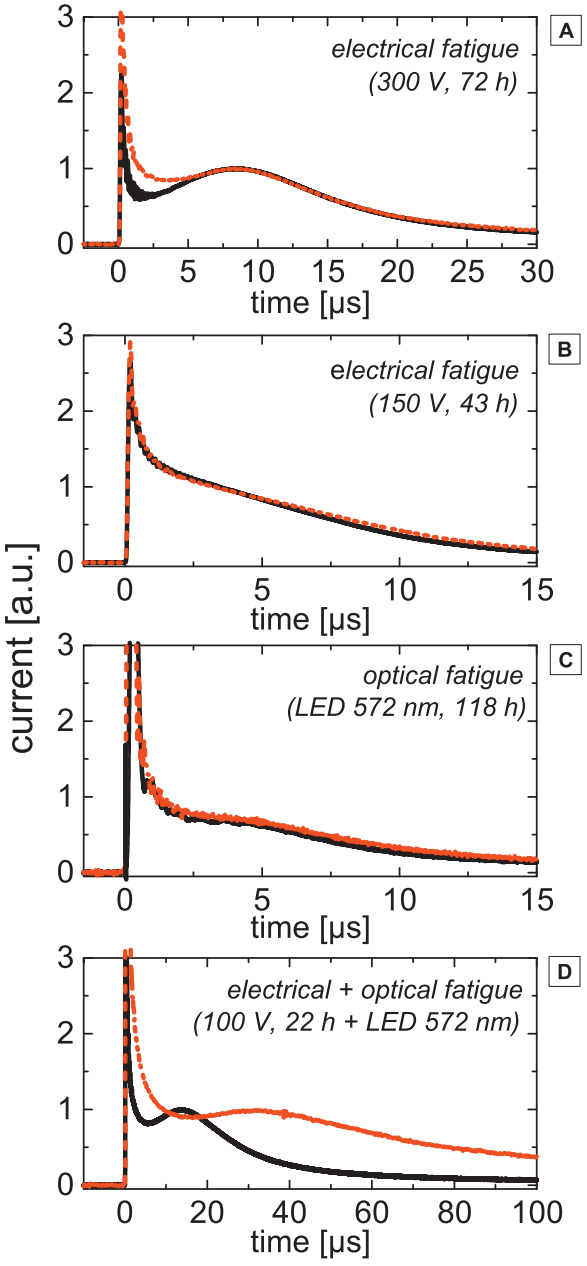


**Fig. 26.** TOF current transients measured before (black solid line) and after (red dashed line) the specified fatiguing method using different hole-only devices: electrical fatigue in the presence of decent injection currents (A), electrical fatigue with low injection currents (B), optical fatigue in open circuit conditions (C), simultaneous electrical and optical fatigue (D). The currents have been scaled to arbitrary values for a better comparability. The respective device structures are: (A) ITO/PEDOT:PSS/$OC_8C_8$-PPV/Au, (B) Al/$OC_8C_8$-PPV/Al, (C) ITO/PEDOT:PSS/$OC_8C_8$-PPV/Al and (D) ITO/PEDOT:PSS/$OC_8C_8$-PPV/Au. For further details see [37,22].

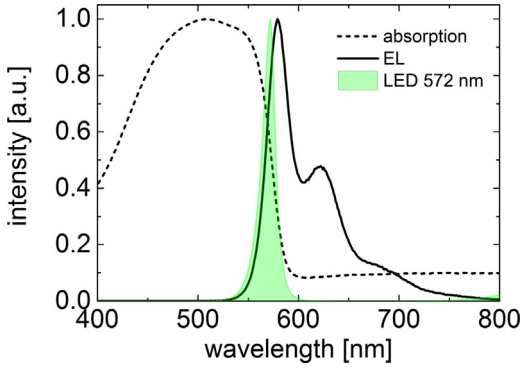


**Fig. 27.** Absorption and electroluminescence (EL) spectra of $OC_8C_8$-PPV. The emission spectrum of the during optical fatigue used LED with a peak wavelength of 572 nm is also included in the diagram.

electrodes with aluminum layers hole injection can be blocked rather effectively (the flowing injection currents are decreased by several orders of magnitude). Thus, the effect of the electric field itself on the hole mobility can be evaluated. It might be the driving force for the slow transport of possible residual ionic species or charged impurities that interfere with the transport of holes in bipolar devices. As illustrated in Fig. 26B the TOF current transients measured before and after electrical fatigue of Al/$OC_8C_8$-PPV/Al devices are again invariant. Both experiments prove that the prolonged electrical operation of unipolar devices does not cause fatigue.[3] This is a strong indication that the presence of electrons in bipolar devices, even though they should be restricted to only a small volume of the PPV-layer (see Fig. 4 in Ref. [22]), is one detrimental factor for the electrical fatigue of PLEDs. Accordingly, it should be possible to detect a change of the transport properties of unipolar, hole-only devices, if electrons can be provided to the device "artificially". This can be realized by irradiating hole-only devices with LEDs emitting at a wavelength that can be absorbed by the polymer thereby optically exciting electrons into LUMO states. The TOF current transients in Fig. 26D confirm that the simultaneous electrical and optical fatigue of a hole-only device drastically changes the transit time for holes. A sole optical fatigue with the same LED on the other hand does not alter the TOF current transients as illustrated in Fig. 26C. These experiments demonstrate clearly that the electrical fatigue of bipolar, hole-dominated PPV-based devices is ruled by the presence of electrons in the device.

An additional outcome of the aforementioned experiments was the proof that self-absorption, the absorption of the light generated by the PLED itself, is indeed also harmful for hole transport. The results presented in Fig. 26C and D were obtained using LEDs with a wavelength of 572 nm, thus lying in the wavelength regime where the absorption and the electroluminescence spectra of the PPV-derivative used overlap (see Fig. 27). Nonetheless, the increase of the hole transit time in the hole-only devices can also be generated using optical irradiation with LEDs of different wavelengths [22,202]. In order to prevent self-absorption in the PLED the use of organic semiconductors with a large Stokes shift would be beneficial. This can be regarded as the introduction of an additional rule for the chemical design of new organic semiconductors for organic light-emitting diodes.

A very important additional influence factor on the lifetime of PLEDs is naturally the magnitude of the electrical stressing, thus the current density in the present study. This translates into a different initial luminance $L_0$ during the lifetime experiment. It is well-known from several empirical studies performed using different organic semiconductors [203–206], that the lifetime scales antiproportional with the initial luminance if a certain acceleration factor $n$ for the latter is taken into account:.

$$t_{50} \times L_0^n = const \tag{3}$$

Using four different current densities for the electrical fatigue of PPV-based PLEDs the respective lifetimes could be extracted and are given in Fig. 28. The thereby calculated scaling law yields an acceleration factor of about $n = -5$ for the tested $OC_3C_8$-PPV devices.

[3] Here the fatigue refers to a change of the hole mobility that is not observed in the described two experiments.

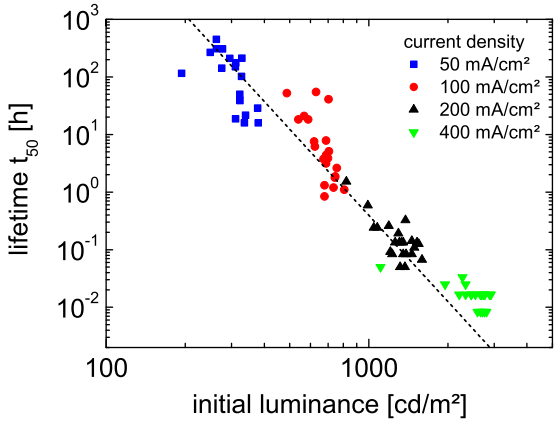


**Fig. 28.** From fatigue experiments extracted lifetimes of PLEDs electrically fatigued at different current densities. The fitting of all data sets using Eq. (3) is depicted as dashed line. The device structure was: ITO/PEDOT:PSS/$OC_3C_8$-PPV/Ca/Al [207].

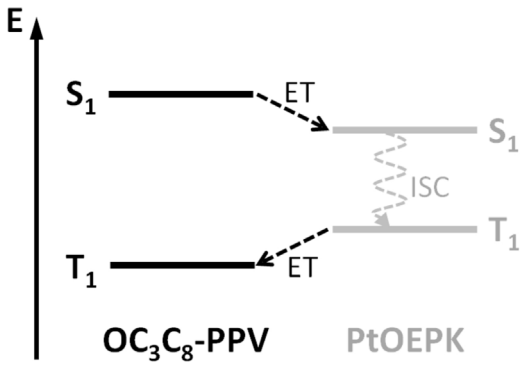


**Fig. 29.** Singlet-to-triplet conversion principle for a $OC_3C_8$-PPV matrix and a PtOEPK guest. A singlet exciton energy transfer (ET) from PPV to PtOEPK takes place, followed by an intersystem crossing (ISC) to the PtOEPK first excited triplet state. The triplet exciton is subsequently transferred back to the PPV due to the energetically lower first excited triplet state.

*4.2.4. Role of triplet excitons in fluorescent devices*

In fluorescent devices only 25% of the created excitons are radiatively decaying singlets. The remaining majority of 75% are triplet excitons that decay non-radiatively, being lost for light emission. Due to this imbalance the efficiency of fluorescent devices is limited to 25% (for 100% efficiency of singlet emission) [208–210]. A well-established method to overcome this limitation is known as triplet harvesting [211–213]. Heavy metal containing molecules (guest, G), often emissive iridium or platinum organometallic complexes [5,65,213–216], are incorporated into the organic matrix (host, H) to weaken the spin selection rules that hinder triplet-to-singlet transitions. As a result the host triplet excitons are collected (or "harvested") at the guest molecules and can decay radiatively by phosphorescence, leading to an increased device efficiency. The precondition for an exciton transfer is that the first excited singlet state of the guest molecules $S_{1,G}$ is energetically lower than the respective $S_{1,H}$-level of the host. The singlet transfer from host to guest is then followed by a fast intersystem crossing (ISC) to the first excited triplet state of the guest molecule $T_{1,G}$. For a subsequent radiative decay of the triplet exciton to its ground state it is mandatory that the first excited triplet state of the guest $T_{1,G}$ is energetically lower than the $T_{1,H}$-level to impede an exciton back-transfer to the matrix molecules.

In fluorescent PPV-based devices no triplet emitters are incorporated and the generated triplet excitons have to decay non-radiatively due to the low intersystem crossing yield in PPV derivatives [217,218]. Consequently, the question arises which influence the high density of non-radiatively recombinating triplet excitons has on the performance and lifetime of PLEDs. To investigate this issue the idea of triplet harvesting has been taken up, choosing an organometallic compound as guest which has a first excited triplet state lying energetically higher than that of the PPV host. Thus, a back-transfer of the triplet exciton to the PPV matrix will occur, thereby increasing the concentration of the triplet excitons in the polymer even more. This approach enabled for example the direct observation of phosphorescence from PPV polymers [219] and has been used recently to improve the external quantum efficiency of organic solar cells [220]. In the present case, a $OC_3C_8$-PPV matrix is blended with small concentrations ($\leq$1 wt%) of the triplet sensitizer molecule platinum(II) octaethylporphyrinketone (PtOEPK) in order to enhance the triplet population.

The energetic scheme of the singlet-to-triplet conversion is illustrated in Fig. 29. A singlet exciton transfer takes place from the polymer to the sensitizer. The energy transfer is followed by a fast intersystem crossing on the sensitizer, facilitated by the presence of the platinum atom. The first excited triplet state of the polymer lies energetically lower than that of PtOEPK, and the triplet exciton is thus transferred back to PPV. The conversion of the singlet excitons to triplets could be verified with photoinduced absorption measurements, where the excited triplet state absorption of sensitized layers increased distinctively in comparison to that of a pristine PPV layer [221]. The singlet-to-triplet conversion is also taking place in electrically driven devices as the loss in PPV singlet excitons is mirrored by a decrease of the electroluminescence with increasing sensitizer content. In addition, no signs of electroluminescence coming from PtOEPK are observed, which indicates a complete energy transfer.

Fig. 30 illustrates the lifetimes of diodes with pristine and sensitized $OC_3C_8$-PPV layers. The $t_{50}$ lifetime of devices with pristine PPV is 160 h, whereas the diodes with a PtOEPK concentration of 0.1 wt% reach a lifetime of only 15 h. Moreover, when the sensitizer concentration is increased to 1 wt%, the $t_{50}$ lifetime drops to only 2 h. This is a 99% decrease in comparison to the lifetime of the diodes with pristine PPV layers [221].

The triplet excitons are found to drastically shorten the lifetime of PPV-based OLEDs. Different processes are presumed to take part in the degradation of the devices. One hypothesis is that the heat that is generated during the non-radiative decay of the triplet excitons is harmful for the diodes. It has been observed that an increased operation temperature accelerates the degradation of organic materials [222,223]. A drastic reduction in device lifetime was reported for MEH-PPV diodes when operating temperature was increased from 30 to 60 °C [223]. It could be possible that the operating temperature within the active layer of the devices

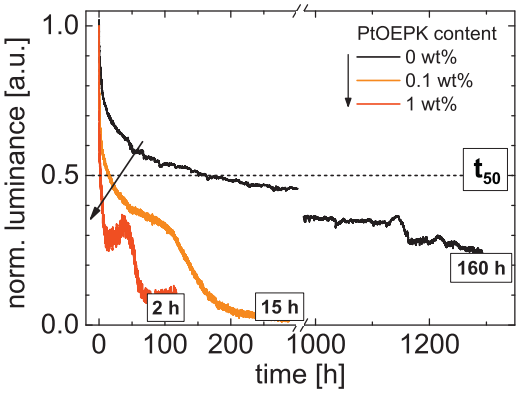


**Fig. 30.** Evolution of the luminance of pristine and sensitized $OC_3C_8$-PPV devices during electrical fatigue at a constant current density of 50 mA/cm². The device structure was: ITO/PEDOT:PSS/$OC_3C_8$-PPV:PtOEPK ($x$ wt%)/Ca/Al.

with an increased triplet exciton concentration rises high enough to accelerate the degradation. However, thermography measurements show an increase of the mean temperature of only about 5 K from room temperature for a pristine device. For a 1 wt% sensitized device, the mean temperature increase is higher with 10 K, but it is questionable whether such a difference in operating temperature is high enough to fully explain the accelerated degradation of the sensitized diodes.

Another hypothesis is that the interaction between polymer triplet excitons and oxygen could play a role in the degradation as well. Due to the long lifetime of triplet excitons, interactions between them and other molecules are likely. An energy transfer from the first excited triplet state of the conjugated polymers to oxygen in triplet state has been commonly observed [38,224–226]. The energy of the polymer triplet state is high enough to excite ground state triplet oxygen to the reactive singlet state. Singlet oxygen is reported to attack the vinylene bond of PPV derivatives. The interaction between oxygen and the PPV and the resulting scission of the polymer chains has been observed even in inert atmosphere with oxygen concentration in the ppm-range. It is therefore relevant also for the present measurements that were performed solely in a glove box. The increased concentration of triplet excitons in the sensitized polymer samples is assumed to lead to an increased interaction with oxygen. However, it is presently not possible to assign the degradation phenomena in triplet exciton enriched devices to a single process.

## 5. Modeling of charge carrier injection and transport

Transport in organic systems is generally described by models based upon hopping of charge carriers between localized states, which are disordered in space and energy (see for example Refs. [227–229] and references therein). These systems are typically wide-band gap disordered semiconductors possessing, as a rule, a relatively narrow intrinsic density-of-states (DOS) distribution without sharp band edges often approximated by a Gaussian function [201]. In addition to the intrinsic DOS distribution, disordered organic semiconductors may exhibit deeper localized states originating from impurities, or from chemical and structural defects. Those states are normally located energetically well below the intrinsic DOS distribution, and therefore, are referred to as deep traps. In general, the energy distributions of such trap states are often assumed to be also of Gaussian shape or exponentially distributed. To simplify the description of transport, a theoretical concept is often applied where charge transport is controlled by carrier jumps to the so-called effective transport energy level [229–233]. This characteristic energy is located within the intrinsic DOS-distribution and is defined as the energy of those sites a charge carrier visits with the highest probability, independently of its energetic starting position. This concept allows one to reduce the description of hopping transport to a multiple trapping formalism [234]. The transport energy then plays the role of the mobility edge in disordered materials [235] and may be used to qualitatively separate mobile and immobile carriers in organic semiconductors. The above simplifications and the commonly simple device geometry in OLEDs, i.e. electrode/organic layer(s)/electrode, allow to describe transport properties of organic devices within the framework of a continuous one-dimensional model utilizing the terms of carrier densities and mean electric field and using generally the continuity equations and a drift-diffusion or drift current, coupled to Poisson equation (see for example Ref. [228]), the approach used also in our simulations. Another important process providing the functionality of OLEDs is the injection of carriers from electrodes into the organic layer in view of a low intrinsic charge carrier density. This process often occurs over an energetic barrier which is defined as a difference between the Fermi level of the injecting electrode and the center of DOS distribution at the HOMO (LUMO) level for hole (electron) injection. However, the description of this process in the literature remains still controversial. Generally, transport and injection properties in organic devices have to be considered simultaneously because of space charge effects.

Arkhipov et al. have analyzed the interplay between charge injection and bulk conductivity using a specific hopping model for injection together with the concepts of the transport energy and trap controlled transport for bulk space charge limited current (SCLC) [236]. Assuming that the unipolar current density in the bulk is determined by drift of mobile carriers, it was shown that space charge in the bulk of the OLED can be a rate-limiting factor at lower temperature even if the injection barrier is high. On the other hand transport is still controlled by the rate of charge injection from a metal contact at higher temperatures even if the injection barrier is relatively low. In Ref. [236], however, single particle hopping process was considered while diffusion was neglected. Taking over a concept of the transport energy and trap controlled transport from this work, diffusion was added to the considerations. To this end the applicability of the Einstein relation between the diffusivity $D$ and the charge-carrier mobility $\mu$ for disordered organic systems should be proven.

The classical Einstein relation $D/\mu = k_BT/q$ was verified by using the generalized form [237] for two typical DOS functions of disordered semiconductors [238,239] (here $k_B$ is the Boltzmann constant, $T$ the absolute temperature, and $q$ the elementary charge). The results for $\mu/D$ in units of $q/k_BT$, assuming a DOS distribution with a Gaussian form and width $\sigma$, are presented in Fig. 31. One can see that the classical Einstein relation remains valid up to the value of $n_c = 10^{18}$ cm$^{-3}$. Qualitatively similar results were obtained for a DOS function, describing a band structure with trap states exponentially distributed from the band edge $E_c$ down. Therefore, it has been established that this relation is valid up to high charge-carrier concentrations relevant to many experimental cases, if the multiple trapping model and the mobility edge concept are assumed.

To study the importance of diffusion on charge carrier densities and distributions inside a diode consisting of an organic layer of thickness $L$ sandwiched between a hole-injecting and an electron-injecting electrode, a very simple model including space charge effects, recombination and diffusion mechanisms were used [240]. The field dependence of the carrier mobilities and the influence of traps were neglected in order to avoid distraction from the main issue. To avoid complications connected with charge injection through a contact barrier, an unimpeded charge injection from ohmic contacts has been considered resulting in SCLC boundary conditions [241]. These boundary conditions assume implicitly importance of diffusion at least in the immediate vicinity to the

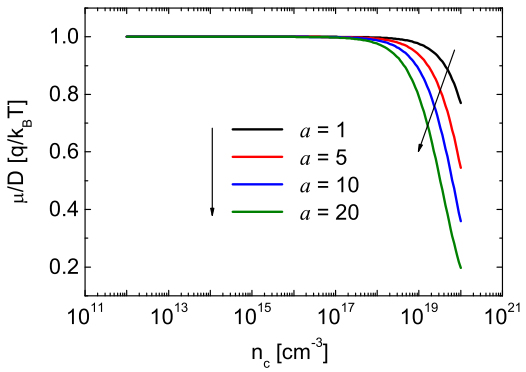


**Fig. 31.** The ratio $\mu/D$ as a function of density of conducting charge carriers, $n_c$, for different values of the dimensionless parameter $a = \sigma/k_BT$ as indicated and total state density $N = 10^{21}$ cm$^{-3}$.

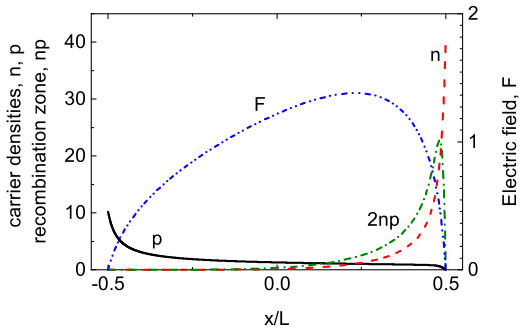


**Fig. 32.** Spatial distributions of charge carrier densities $p$ and $n$ in units of $n_0 = \epsilon\epsilon_0 V/q^2L$, recombination zone $\sim np$ (for clarity $np$ is multiplied by a factor of 2) and electric field $F$ in units of $F_0 = V/L$ for a bipolar OLED with ohmic contacts, the full Langevin recombination and asymmetric mobilities ($\mu_p/\mu_n = 10$), for a voltage of 5 V and a temperature of 300 K.

contacts since the drift current at contacts vanishes together with the field and the whole injection current is due to diffusion only. Fig. 32 presents the calculated spatial distributions of hole and electron densities, $p$ and $n$, respectively, recombination zone and electric field $F$ over a diode with unequal mobilities of holes and electrons, $\mu_p$ and $\mu_n$. The density of the (faster) holes at the injecting electrode is found to be much lower than the density of the (slower) electrons at the corresponding electrode. However, due to the much higher mobility, the hole density is extended deeper into the bulk than the electron density. In previous calculations neglecting diffusion at the electrodes the recombination process was often assumed to take place in the vicinity of both electrodes, even for equal mobilities of holes and electrons [242]. It has been demonstrated that due to diffusion only one recombination zone exists.

For equal mobilities of electrons and holes the recombination zone was found in the center of the device whereas for different mobility values it may be strongly shifted to one of the electrodes, namely toward that side, where the slower charge carriers enter the device. Additionally, diffusion has a strong impact on the current–voltage ($I$–$V$) characteristics in double injection devices. First, due to the inclusion of diffusion, all $I$–$V$ characteristics exhibit temperature dependence. Secondly, the well-known Mott-Gurney law $I \propto V^2$ holds only at sufficiently high voltages and only if recombination is taken into account (see Fig. 33). For small voltages, an ohmic-like behavior is observed in any case. However, if no recombination is assumed, a transition to a $I \propto V^3$ law is obtained for higher voltages.

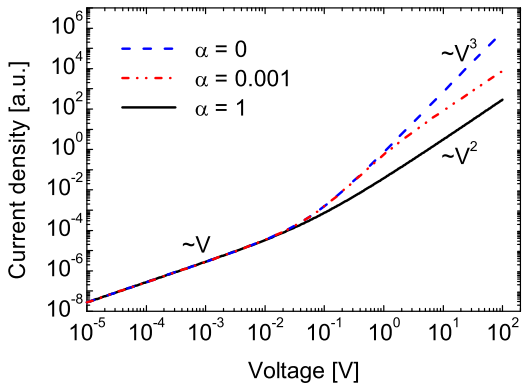


**Fig. 33.** Current–voltage characteristics of a bipolar OLED with ohmic contacts and asymmetric carrier mobilities ($\mu_p/\mu_n = 10$) calculated at temperature $T = 300$ K for different values of recombination parameter $\alpha$. Here $\alpha = 0$ means that the recombination process is not existent, $\alpha = 1$ corresponds to complete Langevin recombination.

### 5.1. Validity of the space charge limited regime: self-consistent consideration in the mean-field regime

The drift-diffusion equation in combination with the Poisson equation involves space-charge effects, but meets the problem of self-consistency in the boundary conditions. The electrostatic potential generated by the injected charge carriers modifies the injection barrier, but on the other hand the amount of charge carriers injected per unit time depends itself on the barrier height. Therefore, a proper description of the injection process by means of the drift-diffusion theory has to involve both the insulator and the conductor sides of the system. For that, a self-consistent continuous description of unipolar injection in insulating media in terms of carrier density and mean field (MF) has been developed [185,243]. The following assumptions were made for the electrode/organic interfaces:

(1) Electrostatic potential is continuous, which means absence of a dipole layer at the interface;
(2) Electric displacement is continuous, which implies absence of a surface charge at the interface;
(3) Electrochemical potential is continuous through the whole system matching particularly at the interface.

To concentrate on injection features, the narrow band approximation for the organic constituent was assumed first neglecting the width $\sigma$ of the Gaussian DOS with respect to the height $\Delta$ of the injection barrier. Also, the Boltzmann statistics of carriers was assumed. Conditions (1–3) together deliver the boundary conditions which connect the values of the field and the carrier density in the organic semiconductor at the interfaces. As a result, the height of injection barriers is modified by the local electric field $F$ at the corresponding interfaces and effective injection barriers may be defined for each electrode as follows (the case of hole injection is exemplarily demonstrated here)

$$\Delta^{\pm}_{eff} = \Delta^{\pm} \pm q l^{\pm}_{TF} F \left(\pm\frac{L}{2}\right) \frac{\epsilon}{\epsilon^{\pm}}. \tag{4}$$

From now on, the minus and plus superscripts denote quantities related to electrodes at the interfaces $x = -L/2$ and $x = L/2$, respectively. Particularly the Thomas–Fermi screening lengths are defined as $l^{\pm}_{TF} = [2\epsilon^{\pm}\epsilon\kappa^{\pm}_{\infty}/(3q^2 p^{\pm}_{\infty})]^{1/2}$ with $p_{\infty}$ and $\kappa_{\infty}$ being, respectively, the equilibrium values of the carrier density and of the chemical potential in the electrode far away from the interface calculated with respect to the bottom of the electrode conduction band. The barrier correction in Eq. (4) is linear in field and may be positive or negative depending on the sign of the local field at the interface. The physical reason for this barrier modification is a contribution of the work done by the mean electric field on electrons in the electrodes.

Considering within the developed MF approach the current–voltage characteristics for a unipolar transport, it was established that there is a crossover from the barrier-dominated behavior at low voltages to the space-charge-dominated behavior at high voltages [185]. Moreover, the SCLC regime prevails over the whole voltage range for injection barriers $\Delta < \Delta_{crit} = k_B T \ln(16LN\kappa_{\infty}/(27 l_{TF} p_{\infty} k_B T))$, with $N$ the density of states for carriers at the HOMO level, revealing $\Delta_{crit}$ between 0.2 eV and 0.35 eV in practical conditions.

The self-consistent MF approach was also applied to simulation of charge carrier injection and transport in a bipolar device [244]. Fig. 34 demonstrates typical spatial dependencies of charge carrier densities $p$ and $n$, recombination zone $\sim np$ and electric field $F$ in a diode structure ITO/OSC/Ca having non-zero, nearly equal injection barriers $\Delta_p$ and $\Delta_n$ for holes and electrons, respectively. To compare with the SCLC case, when the contacts are ohmic and the electric field vanishes at the electrodes, the presented dependencies

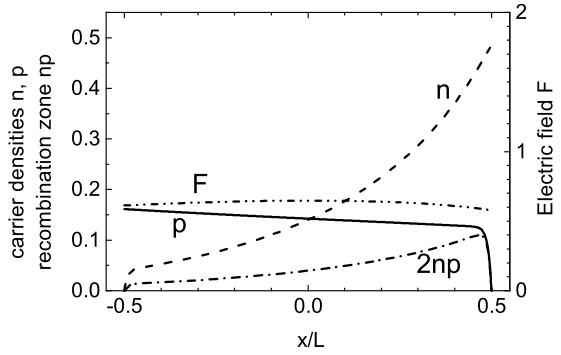


**Fig. 34.** Spatial distribution of charge carrier densities $p$ and $n$ in units of $n_0 = \epsilon\epsilon_0 V/q^2L$, recombination zone $\sim np$ (for clarity $np$ is multiplied by a factor of 2) and electric field $F$ in units of $F_0 = V/L$ for a diode with the full Langevin recombination, asymmetric mobilities ($\mu_p/\mu_n = 10$) and the injection barriers for holes and electrons $\Delta_p = 0.3$ eV and $\Delta_n = 0.27$ eV, respectively, subject to a voltage of 5 V and temperature of 300 K. For more details see text.

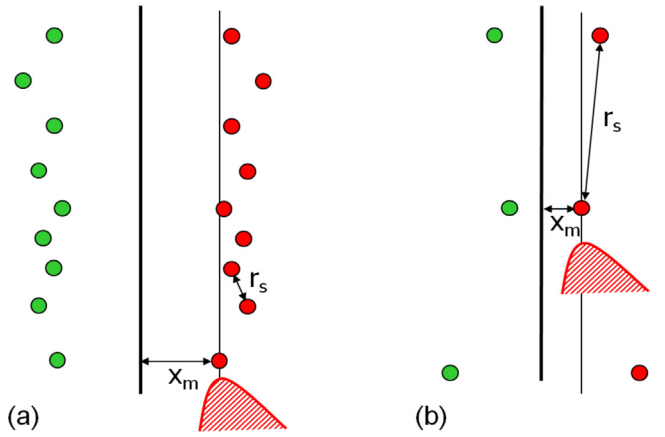


**Fig. 35.** Schematic view of an electrode/organic interface for the cases of high (a) and low (b) density of charge carriers. Injected charges are denoted by red circles and the respective image charges are shown by green circles. Characteristic lengths $x_m$ and $r_s$ are marked as well as the positions of the energy barrier for a single carrier injection are shown. (For interpretation of the references to color in this figure legend, the reader is referred to the web version of this article.)

were calculated for the same voltage and temperature as those shown in Fig. 32. As is seen, non-zero injection barriers strongly depress the densities of injected carriers near the respective electrodes (in the considered case up to two orders of magnitude). At the same time carriers penetrate the organic layer much deeper (almost up to the opposite electrode). Also the electric field changes spatially much weaker and in the case of comparable barrier heights remains almost constant, contrary to the SCLC case where the field spatial distribution is of nearly parabolic shape (see Fig. 32). It should be also noted that the peak position of recombination zone is not affected virtually by non-zero barriers and is determined mainly by the ratio of carrier mobilities.

By varying the heights of injection barriers, it was established that the recombination rate affects the charge carrier and the electric field distributions in the organic layer most strongly when the heights of injection barriers for holes and electrons are comparable. Both the injection barriers and the recombination rate determine the position and shape of the recombination zone and drastically affect the recombination-voltage characteristic of the considered diode structure. In the case of significantly different mobilities of charge carriers it appeared to be possible to maximize the recombination efficiency of a diode by increasing the injection barrier for the faster carriers, which are holes here, thus reducing their concentration.

### 5.2. Schottky lowering of the injection barrier: single-particle versus mean-field regime

The above-considered one-dimensional MF treatment implies averaging of all variables over the plane perpendicular to the injection current density which pertains to relatively high carrier densities and presents a limit opposite to the single-particle injection [236]. At small injection rates, the field-induced reduction of the injection barrier obtained in the MF model is much less than the reduction of the energy barrier due to the single-particle image potential of three-dimensional nature [236,245] which seems to have been confirmed in experiments [228]. Apparently, there are restrictions on application of the mean-field description of the charge injection at low carrier densities. Therefore, the MF model has been extended to allow for the mean-field treatment of charge injection in such a way that the effect of discreteness of charge carriers is accounted for [246].

First, a simple criterion has been looked for which separates the regions of system parameters – voltage and injection barrier – where either the single-particle (SP) or the many-particle, mean-field concept is valid. Adequacy of the MF description of the charge-carrier injection or, alternatively, of the SP picture is determined essentially by the relation between two respective characteristic lengths (Fig. 35). In the first approach, this length is given by an average, three-dimensional distance between the injected charge carriers defined as $r_s = p_s^{-1/3}$, where $p_s$ is the density of these carriers. In the second approach the relevant length is the distance $x_m$ from the plane surface of an electrode to the position of the potential maximum of the energy barrier, $x_m = [q/(16\pi\epsilon\epsilon_0 F(\pm L/2))]^{1/2}$.

Validity of the SP approach is then verified from the point of view of the MF approximation and vice versa. If the density of injected carriers $p_s$ predicted in the continuous consideration is so high that $r_s \ll x_m$ (see Fig. 35(a)), then the presence of many particles between the surface of the electrode and the maximum of the single-particle potential makes the SP approach inappropriate. If, on the other hand, $x_m \ll r_s$ (Fig. 35(b)), then the interaction of a single injected charge carrier with its image is much stronger than with the other distant injected carriers which makes the MF approximation inappropriate. To judge whether the SP approach is relevant, the impact of the deterministic individual image effect should be compared to the impact of the other particles. Due to the stochastic nature of the interaction of the individual particles leading to the energy and force fluctuations, the comparison has been performed in two ways: The mean value or, alternatively, the variance of interaction forces (or energies) have been compared. The two mentioned criteria bring the estimation of the crossover from the SP to the MF domination regime that can be roughly determined by the criterion

$$x_m \simeq 0.2 r_s, \tag{5}$$

which is used in the following analysis.

The above specified microscopic conditions imply restrictions on the macroscopic variables and system parameters which allow for the description of injection in terms of the SP or the MF approach when $x_m$ is smaller or larger than the value given by Eq. (5), respectively. Therefore, the deficiency of the MF approach to the description of the injection within a parameter range where the SP injection mechanism dominates is the missing contribution from the individual image forces on each single charge carrier. This strong but short-range deviation from the mean field near the interface may be accounted for as a dipole layer of a characteristic width $x_m$ as long as the latter distance is much less than $r_s$, which is true in the mentioned region. Indeed, this layer contributes to the shift

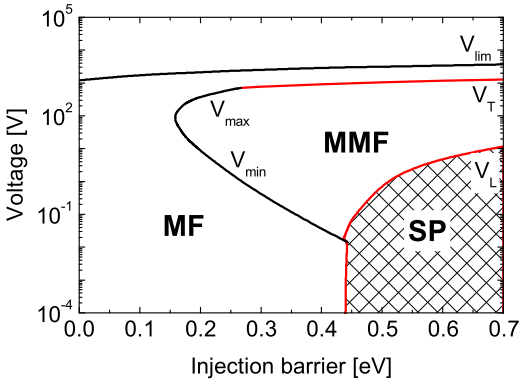


**Fig. 36.** Solid voltage lines $V_{min}$, $V_{max}$, $V_T$, and, partly, $V_L$ outline the MMF area where the MF concept with the boundary condition (7) applies in contrast to the MF area where the boundary condition (7) without the Schottky lowering term holds. The continuous description of charge transport fails completely only in the hatched SP region under the line $V_L$. Line $V_{lim}$ bounds from above the region where the Boltzmann statistics applies.

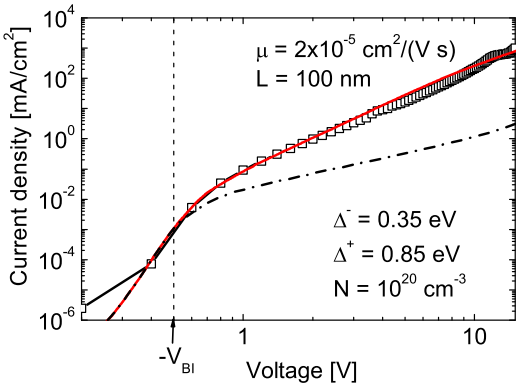


**Fig. 37.** Measured $I$–$V$ characteristic of ITO/$OC_1C_{10}$-PPV/Au structure (squared curve) and its approximations within the MMF (solid curve) and the pure MF (dash-dotted curve) models. The best-fitting parameters in the MMF approach are indicated in the plot.

in energy of each injected charge carrier through the work performed by the individual image force, which results in the shift in the electrostatic potential at the interface given by the Schottky lowering

$$\delta\phi_{Sch} = 2F\left(\pm\frac{L}{2}\right) x_m = \left[\frac{qF(\pm L/2)}{4\pi\epsilon\epsilon_0}\right]^{1/2}. \tag{6}$$

Accounting for that in the mentioned region, requirement (1) of the boundary conditions introduced in the previous Section (continuity of the electrostatic potential) has to be replaced by the condition that the electrostatic potential has a jump at the electrode/organic interface equal to $\delta\phi_{Sch}$. Applying this boundary condition at $x = \pm L/2$, the dipole layer is formally considered as an infinitesimal sheet so that the continuous drift-diffusion and the Poisson equation apply for the organic inner area $-L/2 < x < L/2$. Therefore, at each electrode/organic interface the self-consistent modified mean-field (MMF) boundary condition with the Schottky lowering term

$$\frac{p(\pm L/2)}{N} = \exp\left\{-\frac{\Delta^{\pm}}{k_BT} \mp \frac{ql_{TF}^{\pm}}{k_BT}\left[\frac{\epsilon F(\pm L/2)}{\epsilon^{\pm}} - \frac{j}{\gamma^{\pm}}\right] + \frac{q\delta\phi_{Sch}^{\pm}}{k_BT}\theta\left(0.2r_s^{\pm} - x_m^{\pm}\right)\right\}, \tag{7}$$

is valid, where $\gamma^{\pm}$ denotes the specific conductivities of the electrodes, $j$ is the current density and $\theta$ the Heaviside unit step function. The last term in the exponent of Eq. (7) accounts for the discreteness of charge carriers if $x_m < 0.2r_s$. It thus determines the (MMF) range of the injection barrier and field values where the individual image forces dominate the injection process resulting in the Schottky lowering of injection barriers $q \cdot \delta\phi_{Sch}^{\pm}$ (with $\delta\phi_{Sch}^{\pm}$ from Eq. (6)).

By solving drift-diffusion equations together with the Poisson equation using the boundary condition (7) and the consequent electric field integration over the device the parameter regions may be established where SP and MF approaches respectively apply (see Fig. 36). The $V$–$\Delta$ chart shows voltage and barrier regions where MF and MMF regimes are realized as well as the SP region where the continuous description fails completely because the charge carriers become so sparse in the device that the mean distance between them equals the distance between the electrodes ($r_s = L$).

To evaluate the elaborated MMF model, it has been applied to experimental data obtained on a unipolar device consisting of a single $OC_1C_{10}$-PPV layer of thickness $L = 100$ nm sandwiched between ITO and Au electrodes. In Fig. 37, the measured $I$–$V$ characteristics of the ITO/$OC_1C_{10}$-PPV/Au structure is shown as well as the $I$–$V$ dependencies calculated using different models. One can see that the advanced MMF approach gives a good approximation for the measured $I$–$V$ curve in the wide range of applied voltages with the best-fitting parameters indicated in the figure. At the same time, the dashed curve for the MF approach with the same fitting parameters underestimates the current by orders of the magnitude at high voltages. Note that the widely used Crowell and Sze model [247,248] fails to describe the $I$–$V$ characteristic at voltages below $-V_{bi}$, where $-V_{bi}$ is the voltage drop in the case of $j = 0$, i.e. the built-in potential given by the difference of the electrode's work functions.

### 5.3. Account for distributed DOS and role of traps: temperature dependence

Next, the self-consistent MMF approach was extended to account for a realistic DOS shape of the organic material which becomes important when using different temperatures [249]. The charge transport in the semiconductor/OSC/conductor diode structure was modeled using the transport energy concept in the following way: Charge transport is provided by mobile carriers with a constant mobility where all temperature dependencies in the transport description result from the Fermi distribution of carriers [250,251] and from the temperature dependence of the transport energy [236]. The consideration has been focused on the influence of the injection barrier heights and DOS parameters on the $I$–$V$ characteristics. As an example, a system was studied where only holes were injected from an ITO electrode into the organic semiconductor, for simplicity.

The organic semiconductor is characterized by a DOS represented here as a superposition of two Gaussian DOS: The intrinsic DOS represents the highest occupied molecular level (HOMO band) and the second one describes the spatially and energetically distributed trap states. The total DOS distribution then can be written as [244]

$$g(E) = \frac{P_c}{\sqrt{2\pi}\sigma_c}\exp\left(-\frac{E^2}{2\sigma_c^2}\right) + \frac{P_t}{\sqrt{2\pi}\sigma_t}\exp\left[-\frac{(E-E_t)^2}{2\sigma_t^2}\right], \tag{8}$$

where $E_t$ denotes the average trap energy, $\sigma_c$ and $\sigma_t$ are the widths of the intrinsic and trap DOS parts, $P_c$ and $P_t$ are the numbers of intrinsic states and traps, respectively (notice that the level $E = 0$ coincides with the DOS maximum of the HOMO band). Spatial

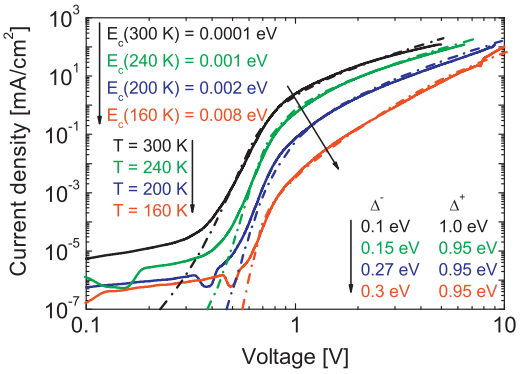


**Fig. 38.** Measured *I–V* characteristics (solid curves) of the ITO/P3HT/Al diode at different temperatures [251] and their fitting (dashed curves) with the OSC model parameters: $\mu = 6.7 \cdot 10^{-4}$ cm$^2$ V$^{-1}$ s$^{-1}$; $P_c = 10^{21}$ cm$^{-3}$; $P_t = 5 \cdot 10^{15}$ cm$^{-3}$; $\sigma_c = 0.035$ eV; $\sigma_t = 0.02$ eV; $E_t = 0.5$ eV.

distributions of the charge carrier density $p$ and the electric field $F$ in the organic semiconductor are described by the system of equations

$$k_B T\mu \frac{dp_c(x)}{dx} - q\mu p_c(x)F(x) = -j, \tag{9}$$

$$\frac{dF(x)}{dx} = \frac{q}{\epsilon\epsilon_0} p(x). \tag{10}$$

where the total density of charge carriers $p(x) = p_c(x) + p_t(x)$ is the sum of mobile and immobile carrier densities, which are separated by the effective energy of the transport level $E_c$ as

$$p_c(x) = \int_{-\infty}^{E_c} g(E) f_p(E) dE,\ p_t(x) = \int_{E_c}^{\infty} g(E) f_p(E) dE, \tag{11}$$

with $f_p(E) = \{\exp[(\kappa(x) + q\phi(x) - E)/(k_B T)] + 1\}^{-1}$ being the Fermi–Dirac distribution of holes. Assuming the Boltzmann statistics for the mobile carriers, the total density of carriers is

$$p(x) = p_c(x) + p_c(x) \int_{E_c}^{\infty} \frac{g(E)dE}{N_c \exp(-E/k_B T) + p_c(x)}, \tag{12}$$

where $N_c$ is interpreted as the effective total number of states available for mobile carriers in the transport band of the organic semiconductor. The nonlinear differential equations (9) and (10) with $p(x)$ from Eq. (12) supplied with the boundary conditions from Eq. (7) have been numerically solved. Knowledge about the spatial distribution of the electric field gives access to the voltage drop $V$ across the system for a given current density $j$, which follows by direct integration of the field over the device thickness.

To test the presented model, it has been applied to the experimental *I–V* characteristics measured on a unipolar device consisting of a single poly(3-hexylthiophene) (P3HT) layer of thickness $L = 125$ nm sandwiched between ITO and Al electrodes. It was deduced from experiments [251] that the total DOS in P3HT consists of the superposition of two Gaussian peaks, which is similar to Eq. (8). Fig. 38 depicts the *I–V* characteristics of the ITO/P3HT/Al structure from Ref. [251] measured at different temperatures along with the best fits calculated with the OSC model parameters indicated.

First, by fitting the $T = 300$ K curve, the best values for the DOS parameters and the carrier mobility were established. Next, by fitting the curves for the other temperatures, these model parameters remained unchanged and only the barrier heights $\Delta^{\pm}$ and the transport energy $E_c$, were allowed to vary with temperature. One can see that the calculations satisfactorily reproduce the magnitude and the general form of the *I–V* characteristics in a wide range of applied voltages and at temperatures between 160 K and 300 K with the fitting parameters indicated in the figure. The remarkable deviation of the theory from the experiment in the low-voltage parts of the *I–V* characteristics (below $-V_{bi}$) is explained by a parallel leakage current which was not taken into account in the model presented.

It should be noted that the obtained fitting clearly emphasizes the essential role of the self-consistent boundary conditions in the proposed theoretical model. In Ref. [251], the experimental *I–V* curves have been simulated within the basically similar mobility edge concept, but using the temperature-independent transport energy $E_c = 0$ and the space-charge limited boundary conditions of $F(\pm L/2) = 0$. Here, the simulation has revealed a less satisfactory agreement between the calculated and experimental curves and an unreasonably low number of intrinsic states on the order of $10^{18}$ cm$^{-3}$ in contrast to the number of $10^{21}$ cm$^{-3}$ obtained in our simulations. Finally, compared with the popular extended Gaussian disorder model which involves both field and carrier density dependencies of the effective average mobility of the whole ensemble of carriers [252,253], the present approach has a comparable number of fitting parameters and gives a similar fitting accuracy.

### 5.4. Beyond the transport level and the constant carrier mobility concepts

To this end the concept of transport level has been used and it was assumed that all mobile carriers have the same constant mobility. As was shown above, this approach is quite well for fitting of the current–voltage characteristics of organic devices, especially if *I–V* curves reach $V^2$ behavior at high voltages. However, if the experimental *I–V* curves reveal steeper voltage dependencies, the constant mobility assumption seems to be insufficient and alternative concepts of charge transport should be involved into the consideration. By now, the most advanced approaches are the extended Gaussian disorder model (EGDM) [252,253] being adequate for polymeric semiconductors and its modification, the correlated Gaussian disorder model (CGDM) [254] applicable to small molecule organic semiconductors. In both approaches, all carriers in intrinsic DOSs are considered mobile and their effective drift mobility is assumed to be dependent on the temperature $T$, on the carrier density $p$ (or $n$) and, in general, on the electric field $F$. For these $\mu(T, p, F)$ dependencies quite cumbersome expressions were suggested (see Refs. [252–254]) with which, however, the EGDM and CGDM approaches have demonstrated a good ability to simulate the *I–V* characteristics of different organic devices. Such approximations for the carrier mobility may be easily incorporated in the above-described MMF model (Eqs. (9) and (10) with the boundary condition from Eq. (7)). The MMF approach extended in this way is easy applicable to simulation of hole transport in unipolar diodes.

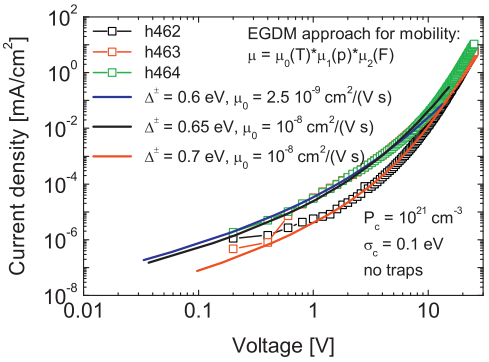


**Fig. 39.** Measured *I–V* characteristics (curves with squares) of the hole-only ITO/$OC_1C_{10}$-PPV/Au diodes at room temperature and their best fitting (solid curves) with the OSC model parameters. (For interpretation of the references to color in this figure legend, the reader is referred to the web version of this article.)

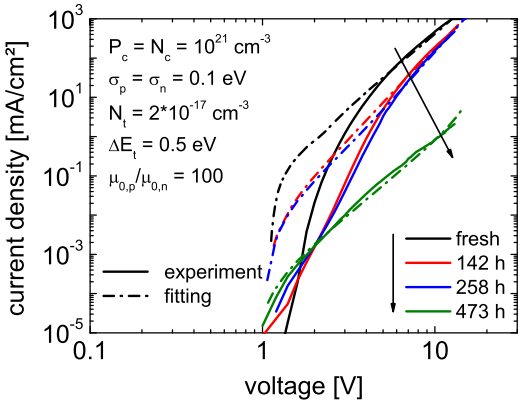


**Fig. 40.** Measured *I–V* characteristics (solid curves) of a bipolar ITO/PEDOT:PSS/$OC_3C_8$-PPV/Ca/Al diode that was fatigued at a constant current density of 5 mA/cm² for different periods at room temperature and their best fitting curves (dash-dotted). The thickness of the organic layer *L* was 130 nm. The OSC model parameters are indicated in the figure and the fitting parameters are given in Table 2.

**Table 2**
The fitting parameters for the *I–V* characteristics of an electrically fatigued bipolar ITO/PEDOT:PSS/$OC_3C_8$-PPV (130 nm)/Ca/Al diode shown in Fig. 40.

| Fatigue time [h] | $\Delta_p$ [eV] | $\Delta_n$ [eV] | $\mu_{0,p}$ [cm² V⁻¹ s⁻¹] |
|---|---|---|---|
| 0 (fresh) | 0.55 | 0.55 | $2.20 \cdot 10^{-6}$ |
| 142 | 0.60 | 0.60 | $1.65 \cdot 10^{-6}$ |
| 258 | 0.60 | 0.60 | $1.30 \cdot 10^{-6}$ |
| 473 | 0.60 | 0.80 | $5.90 \cdot 10^{-8}$ |

Fig. 39 depicts the *I–V* characteristics of three ITO/$OC_1C_{10}$-PPV/Au diodes with the same thickness of organic layer $L = 130$ nm measured at the room temperature along with their best fits calculated using the EGDM approximation for the hole mobility [252,253] and the organic semiconductor's Gaussian DOS parameters indicated.

The actual, most advanced model can also be implemented for the description of bipolar transport and recombination in diode structures and is particularly applicable for tracing the evolution of system parameters during fatigue. To this end electronic traps should be additionally introduced into the model since they are expected to be relevant for the observed fatigue features as discussed above in Section 4.1.2. Thus, a single trap level characterized by its density of states $N_t$ and depth $\Delta E_t$ with respect to the peak of the LUMO band was added to the model described in Section 5.3. Otherwise the bipolar transport equations are the same as in the drift-diffusion approach [244]. Current–voltage characteristics calculated within this model with a recombination rate assumed to be $10^{-2}$ of the maximum Langevin recombination rate were compared with virgin and differently fatigued PLEDs of ITO/PEDOT:PSS/$OC_3C_8$-PPV/Ca/Al structure (see Fig. 40). For this comparison the experimental curves have been corrected for the Ohmic currents usually observed at low voltages (<1 V) and attributed to leakage currents.

Appropriate parameter values for the fitting are presented in Fig. 40 and Table 2. In contrast to the unipolar case (Fig. 39), the theoretical results given by the dash-dotted lines remarkably deviate in the low-voltage region from the experimental data shown by solid lines but deliver satisfactory description at higher voltages. The gradual increase of injection barriers and reduction of charge carrier mobilities $\mu_{0,p}$ and $\mu_{0,n}$ with progressing fatigue, as presented in Table 2, in principle plausibly delineate degradation of the device. The observed increase of the injection barriers (corresponding to an increase of work functions) indicates a possible reaction of the electrodes with either still present residual bromine of an uncompleted dehydrohalogenation reaction (see Section 4.1.2) or with oxygen from ITO (see Section 3.5) or from the glove box environment. In addition, the observed decrease of the hole mobility could be due to an increased energetic disorder and a changing morphology with ongoing fatigue as discussed in Section 4.2.1. Further refinement of the model requires experimental evidences on what particular constitutional parameters are affected by electrical fatigue. Contrary to the example above where only the hole mobility was changed while keeping the ratio between hole and electron mobility constant both charge carrier mobilities, their densities of states and trap distributions, the injection barriers, the recombination rate, etc. have to be considered in order to fully describe experimental curves for electrically fatigued devices.

## 6. Summary

The detailed understanding of the processes governing OLED operation and especially its operational degradation is remaining in the focus of recent investigations. Even though light-emitting diodes have been successfully introduced into certain application fields, the basic properties of the involved materials as well as the interplay of materials at interfaces are still not fully understood:

*(i) Materials in OLEDs*: The current manuscript focused on the organic semiconductor poly(*p*-phenylene-vinylene). Gilch-synthesized PPV-derivatives were successfully prepared and evaluated in PLEDs. The mechanism of the Gilch reaction was proven to be radical and the origin of defects formed in PPVs. It was found that the halogen defects are the main limiting factor for the PLED lifetimes. Due to the slow dehydrohalogenation reaction the elimination of halogen traces from the polymer backbone takes days. If this is considered during material synthesis, long-lived PLEDs with lifetimes of several hundreds of hours can be produced.

As for the common anode material ITO, the knowledge on bulk defect and surface properties of $In_2O_3$ and ITO was reported. The latter can exhibit carrier concentrations of up to $\sim 10^{21}$ cm$^{-3}$ with a typical doping concentration of 10 mol% $SnO_2$. The electron concentration is limited by self-compensation with oxygen interstitials as compensating acceptors. ITO does therefore exhibit an over-stoichiometric amount of oxygen where the oxygen interstitials can be easily exchanged at the surface even though oxygen diffusion is rather slow for temperatures below 200 °C. It is therefore unlikely that oxygen released from ITO contributes significantly to electrical fatigue of OLEDs. A degradation of interface properties and an enhanced oxygen release due to high electric fields during device operation can, however, not be excluded at present. The ionization potential and work function depend strongly on surface orientation. Except for strongly reducing or strongly oxidizing conditions, the (1 1 1) surface has the lowest surface energy and ionization potential A significant enhancement of ionization potential and work function upon surface oxidation is expected for the (1 0 0) surface orientation. The orientation dependence of the work function is expected to lead to a spatially inhomogeneous charge injection which is likely to be the origin of hot spot formation.

*(ii) Interplay between the materials in the device*: During electrical fatigue the injection barriers might change or charge carrier injection might be impeded by the formation of interlayers. As for the charge carrier transport in PPV it was shown that the hole mobility strongly depends on the morphological order of the polymer chains. This order is influenced by the symmetry of the side chains attached to the backbone and by the molecular weight of the polymer. Experiments with three different PPV derivatives revealed that electrical fatigue decreases the hole mobility and induces also a transition from non-dispersive to dispersive transport. The impact of non-radiatively decaying triplet excitons on device fatigue has

been evaluated by increasing the triplet exciton density on the PPV chains incorporating a triplet sensitizer molecule in low concentrations (0.1–1 wt%). The results are drastically shortened lifetimes of the PLEDs. Even though different mechanisms are discussed, it is presently not possible to assign the degradation of triplet-enriched devices to one single mechanism.

In order to better understand the physics in OLEDs, a self-consistent continuous model of stationary injection and transport of charge carriers in insulating media with account for discreteness of the carriers during injection has been developed. The model was satisfactorily applied to the description of unipolar or bipolar diodes at different temperatures considering a Gaussian DOS distribution for mobile carriers and shallow trap states. It can be easily generalized to more complicated approximations for both carrier-density and electric field dependencies of mobility and diffusivity. Using injection barrier heights, mobility of carriers and DOS shapes as fitting parameters, application of the model to fatigue measurements will allow to trace changes of system properties and allows to draw conclusions on mechanisms of device degradation. However, a better experimental insight is needed to assess the multiple parameters which are unavoidable for a realistic model description.

Finally, it can be stated that further knowledge on the functionality and electrical fatigue induced changes of materials and system parameters in OLEDs can only be gained by a collaborative approach where scientists from different fields work hand in hand. Additionally, it has to be kept in mind that especially degradation is strongly material dependent, thus complicating the development of a general model for device degradation in small-molecular and polymeric OLEDs. In particular, the presence of phosphorescent emitters and their operational stability was not considered here. Nevertheless, it seems that consensus has been reached in the community that the utilization of highly pure organic semiconductors and a controlled and reproducible processing of the materials are necessary preconditions to obtain well-behaving devices.

## Acknowledgements

The financial support from the German Science Foundation (DFG) of the collaborative research center SFB 595 “Electrical fatigue in functional materials” for three funding periods (2003–2014) is gratefully acknowledged. The authors thank all former and present colleagues that contributed to this work: P. Ágoston, V.I. Arkhipov†, P. Erhart, A. Fey, A. Fleissner, Y. Gassenbauer, M. Hohmann, H. Janning, J. Langecker, C. Melzer, F. Neumann†, S. Nickel, M. Preuss, V. Rittscher, R. Sander, R. Savikoski, R. Schmechel, M. Schütz, T. Schwalm, K. Stegmaier, A. Wachau and J. Wiesecke.

## References

[1] D. Fyfe, Nat. Photonics 3 (2009) 453–455.
[2] R. Mertens, The OLED Handbook: A Guide to OLED Technology, Industry & Market, 2012.
[3] F. So, B. Krummacher, M.K. Mathai, D. Poplavskyy, S.A. Choulis, V.E. Choong, J. Appl. Phys. 102 (2007) 091101.
[4] T.W. Lee, T. Noh, H.W. Shin, O. Kwon, J.J. Park, B.K. Choi, M.S. Kim, D.W. Shin, Y.R. Kim, Adv. Funct. Mater. 19 (2009) 1625–1630.
[5] L.A. Duan, L.D. Hou, T.W. Lee, J.A. Qiao, D.Q. Zhang, G.F. Dong, L.D. Wang, Y. Qiu, J. Mater. Chem. 20 (2010) 6392–6407.
[6] Q. Fu, J.S. Chen, C.S. Shi, D.G. Ma, ACS Appl. Mater. Interfaces 4 (2012) 6579–6586.
[7] B. Geffroy, P. Le Roy, C. Prat, Polym. Int. 55 (2006) 572–582.
[8] S. Schmidbauer, A. Hohenleutner, B. König, Adv. Mater. 25 (2013) 2114–2129.
[9] F. So, D. Kondakov, Adv. Mater. 22 (2010) 3762–3777.
[10] S. Nowy, W. Ren, A. Elschner, W. Loevenich, W. Bruetting, J. Appl. Phys. 107 (2010) 054501.
[11] T.D. Schmidt, D.S. Setz, M. Flaemmich, B.J. Scholz, A. Jaeger, C. Diez, D. Michaelis, N. Danz, W. Bruetting, Appl. Phys. Lett. 101 (2012) 103301.
[12] Q. Wang, Y. Luo, H. Aziz, J. Appl. Phys. 107 (2010) 084506.
[13] R. Huber, F. Witt, H. Borchert, E. von Hauff, S. Heun, H. Buchholz, J. Parisi, J. Appl. Phys. 113 (2013) 023104.
[14] H. Aziz, Z.D. Popovic, Chem. Mater. 16 (2004) 4522–4532.
[15] S. Gardonio, L. Gregoratti, P. Melpignano, L. Aballe, V. Biondo, R. Zamboni, M. Murgia, S. Caria, M. Kiskinova, Org. Electron. 8 (2007) 37–43.
[16] S.F. Lim, W. Wang, S.J. Chua, Mater. Sci. Eng. B: Solid State Mater. Adv. Technol. 85 (2001) 154–159.
[17] R. Phatak, T.Y. Tsui, H. Aziz, J. Appl. Phys. 111 (2012) 054512.
[18] L.M. Do, K.J. Kim, T. Zyung, H.K. Shim, J.J. Kim, Appl. Phys. Lett. 70 (1997) 3470–3472.
[19] S.H. Kim, S.C. Lim, J.H. Lee, C.H. Ku, J.B. Koo, Y.S. Yang, T. Zyung, Appl. Phys. Lett. 89 (2006) 022101.
[20] Y.F. Liew, H. Aziz, N.X. Hu, H.S.O. Chan, G. Xu, Z. Popovic, Appl. Phys. Lett. 77 (2000) 2650–2652.
[21] H. Aziz, G. Xu, J. Phys. Chem. B 101 (1997) 4009–4012.
[22] K. Stegmaier, A. Fleissner, H. Janning, S.V. Yampolskii, C. Melzer, H. von Seggern, J. Appl. Phys. 110 (2011) 034507.
[23] A. Fleissner, K. Stegmaier, C. Melzer, H. von Seggern, T. Schwalm, M. Rehahn, Chem. Mater. 21 (2009) 4288–4298.
[24] A. Fleissner, H. Schmid, C. Melzer, H. von Seggern, Appl. Phys. Lett. 91 (2007) 242103.
[25] D.Y. Kondakov, W.C. Lenhart, W.F. Nichols, J. Appl. Phys. 101 (2007) 024512.
[26] S. Scholz, R. Meerheim, B. Luessem, K. Leo, Appl. Phys. Lett. 94 (2009) 043314.
[27] D.Y. Kondakov, R.H. Young, J. Appl. Phys. 108 (2010) 074513.
[28] I.R. de Moraes, S. Scholz, B. Luessem, K. Leo, Org. Electron. 12 (2011) 341–347.
[29] I.R. de Moraes, S. Scholz, B. Luessem, K. Leo, Org. Electron. 13 (2012) 1900–1907.
[30] C. Shen, A. Kahn, J. Schwartz, J. Appl. Phys. 89 (2001) 449–459.
[31] H. Ding, Y. Gao, Appl. Surf. Sci. 252 (2006) 3943–3947.
[32] J. Hwang, A. Wan, A. Kahn, Mater. Sci. Eng. R: Rep. 64 (2009) 1–31.
[33] Y.L. Gao, Mater. Sci. Eng. R: Rep. 68 (2010) 39–87.
[34] T.P. Nguyen, S.H. Yang, P. Le Rendu, C. Renaud, Phys. Stat. Solid. C 6 (2009) 1856–1861.
[35] H. Kanaan, P. Jolinat, G. Ablart, P. Destruel, C. Renaud, C.W. Lee, T.-P. Nguyen, Org. Electron. 11 (2010) 1047–1052.
[36] M. Petrosino, A. Rubino, Org. Electron. 12 (2011) 1159–1165.
[37] K. Stegmaier, Elektrische Ermüdung polymerbasierter organischer Leuchtdioden (Ph.D. thesis), Technische Universität Darmstadt, Materials Science Department, 2011.
[38] R. Scurlock, B. Wang, P. Ogilby, J. Sheats, R. Clough, J. Am. Chem. Soc. 117 (1995) 10194–10202.
[39] J. Chang, Y.-J. Yu, J.H. Na, J. An, C. Im, D.-H. Choi, J.-I. Jin, S.H. Lee, Y.K. Kim, J. Polym. Sci. B 46 (2008) 2395–2403.
[40] I.D. Parker, Y. Cao, C.Y. Yang, J. Appl. Phys. 85 (1999) 2441–2447.
[41] R. Pacios, A.J. Chatten, K. Kawano, J.R. Durrant, D.D.C. Bradley, J. Nelson, Adv. Funct. Mater. 16 (2006) 2117–2126.
[42] S. Onda, H. Kobayashi, T. Hatano, S. Furumaki, S. Habuchi, M. Vacha, J. Phys. Chem. Lett. 2 (2011) 2827–2831.
[43] E. Palacios-Lidon, E. Escasain, E. Lopez-Elvira, A.M. Baro, J. Colchero, Sol. Energy Mater. Sol. Cells 117 (2013) 15–21.
[44] S. Kappaun, C. Slugovc, E.J.W. List, Adv. Polym. Sci. 212 (2008) 273–292.
[45] A. Berntsen, Y. Croonen, C. Liedenbaum, H. Schoo, R.-J. Visser, J. Vleggaar, P. van de Weijer, Opt. Mater. 9 (1998) 125–133.
[46] H. Aziz, Z.D. Popovic, N.X. Hu, A.M. Hor, G. Xu, Science 283 (1999) 1900–1902.
[47] Z.D. Popovic, H. Aziz, N.X. Hu, A. Ioannidis, P.N.M. dos Anjos, J. Appl. Phys. 89 (2001) 4673–4675.
[48] J. Steiger, S. Karg, R. Schmechel, H. von Seggern, Synth. Met. 122 (2001) 49–52.
[49] S. Kim, C. Hsu, C. Zhang, H. Skulason, F. Uckert, D. LeCloux, Y. Cao, I. Parker, J. Inform. Display 5 (2004) 14–18.
[50] D.Y. Kondakov, J. Appl. Phys. 97 (2005) 024503.
[51] C. Renaud, T.-P. Nguyen, J. Appl. Phys. 106 (2009) 053707.
[52] A. Elschner, F. Bruder, H.W. Heuer, F. Jonas, A. Karbach, S. Kirchmeyer, S. Thurm, Synth. Met. 111 (2000) 139–143.
[53] S. Kirchmeyer, K. Reuter, J. Mater. Chem. 15 (2005) 2077–2088.
[54] M.P. de Jong, L.J. van IJzendoorn, M.J.A. de Voigt, Appl. Phys. Lett. 77 (2000) 2255–2257.
[55] K. Fehse, R. Meerheim, K. Walzer, K. Leo, W. Loevenich, A. Elschner, Appl. Phys. Lett. 93 (2008) 083303.
[56] S.T. Lee, Z.Q. Gao, L.S. Hung, Appl. Phys. Lett. 75 (1999) 1404–1406.
[57] J. Youn, S. Baek, H. Kim, D. Nam, Y. Lee, J. Lee, J. Jang, J. Mater. Chem. C 1 (2013) 3250–3254.
[58] A. Turak, RSC Adv. 3 (2013) 6188–6225.
[59] N. Koch, ChemPhysChem 8 (2007) 1438–1455.
[60] J.H. Cook, H.A. Al-Attar, A.P. Monkman, Org. Electron. 15 (2014) 245–250.
[61] J.H. Burroughes, D.D.C. Bradley, A.R. Brown, R.N. Marks, K. Mackay, R.H. Friend, P.L. Burns, A.B. Holmes, Nature 347 (1990) 539–541.
[62] G. Inzelt, Conducting Polymers: A New Era in Electrochemistry, Springer, Berlin, 2008.
[63] W. Bruetting, Physics of Organic Semiconductors, Wiley-VCH, Weinheim, 2005.
[64] U. Muellen, K. Scherf, Organic Light Emitting Devices: Synthesis, Properties and Applications, Wiley-VCH, Weinheim, 2005.
[65] H. Yersin, Highly Efficient OLEDs With Phosphorescent Materials, Wiley-VCH, Weinheim, 2007.
[66] C. Brabec, U. Scherf, V. Dyakonov, Organic Photovoltaics: Materials, Device Physics, and Manufacturing Technologies, Wiley-VCH, Weinheim, 2008.

[67] D.A. Bernards, R.M. Owens, G. Malliaras, Organic Semiconductors in Sensor Applications, Springer-Verlag, 2008.
[68] T. Schrader, Creative Chemical Sensor Systems, Springer, Berlin, 2007.
[69] F. Koch, W. Heitz, Macromol. Chem. Phys. 198 (1997) 1531–1544.
[70] H. Katayama, M. Nagao, T. Nishimura, Y. Matsui, K. Umeda, K. Akamatsu, T. Tsuruoka, H. Nawafune, F. Ozawa, J. Am. Chem. Soc. 127 (2005) 4350–4353.
[71] H. Katayama, M. Nagao, T. Nishimura, Y. Matsui, Y. Fukuse, M. Wakioka, F. Ozawa, Macromolecules 39 (2006) 2039–2048.
[72] T. Yamamoto, Y. Hayashi, A. Yamamoto, Bull. Chem. Soc. Jpn. 51 (1978) 2091–2097.
[73] H. Kawahara, I. Otsuka, Preparation of polyarylenevinylene (Patent JP57207618), 1982, URL: http://www.sumobrain.com/patents/JP57207618.html
[74] H. Kawahara, I. Otsuka, Preparation of polyarylenevinylene (Patent JP57207619), 1982, URL: http://www.sumobrain.com/patents/JP57207619.html
[75] Z.N. Bao, Y.M. Chen, R.B. Cai, L.P. Yu, Macromolecules 26 (1993) 5281–5286.
[76] H.G. Gilch, W.I. Wheelwri, J. Polym. Sci. [A1] 4 (1966) 1337.
[77] L. Rajaraman, M. Balasubramanian, M.J. Nanjan, Curr. Sci. 49 (1980) 101–102.
[78] A.W. Cooke, K.B. Wagener, Macromolecules 24 (1991) 1404–1407.
[79] R.A. Wessling, J. Polym. Sci.: Polym. Sympos. 72 (1985) 55–66.
[80] D.J. Vanderzande, A.C. Issaris, M.J. VanderBorght, A.J. VanBreemen, M.M. deKok, J.M. Gelan, Abst. Pap. Am. Chem. Soc. 213 (1997) 49–Orgn.
[81] H. Roex, P. Adriaensens, D. Vanderzande, J. Gelan, Macromolecules 36 (2003) 5613–5622.
[82] F.C. Krebs, R.B. Nyberg, M. Jorgensen, Chem. Mater. 16 (2004) 1313–1318.
[83] N. Vilbrandt, S. Nickel, S. Immel, M. Rehahn, K. Stegmaier, C. Melzer, H. von Seggern, Synthesis of Polymers: New Structures and Methods, Wiley-VCH, Weinheim, 2012.
[84] Y. Ohmori, M. Uchida, K. Muro, K. Yoshino, Japan. J. Appl. Phys.: Lett. 30 (1991) L1941–L1943.
[85] C. Towns, R. O'Dell, S. O'Connor, Polymers, their preparation and uses (Patent US6861502), 2005.
[86] P. Chen, G.Z. Yang, T.X. Liu, T.C. Li, M. Wang, W. Huang, Polym. Int. 55 (2006) 473–490.
[87] J. Langecker, M. Rehahn, Macromol. Chem. Phys. 209 (2008) 258–271.
[88] J. Sakamoto, M. Rehahn, G. Wegner, A.D. Schluter, Macromol. Rapid Commun. 30 (2009) 653–687.
[89] S. Braese, A. de Meijere, Metal-Catalyzed Cross-Coupling Reactions, Wiley-VCH, Weinheim, 2004.
[90] M. Preuss, Konstitutionelle Defekte in Poly(p-phenylenvinylen)en aus Heck- und Suzuki-Polykondensationen (Ph.D. thesis), Technische Universität Darmstadt, Chemistry Department, 2010.
[91] M.W. Brandt, J.E. Mulvaney, H.K. Hall, Macromolecules 21 (1988) 1553–1556.
[92] R. Garay, R.W. Lenz, Makromol. Chem. – Macromol. Chem. Phys. 15 (1989) 1–7.
[93] B.R. Hsieh, Abst. Pap. Am. Chem. Soc. 202 (1991) 13–Poly.
[94] F.R. Denton, A. Sarker, P.M. Lahti, R.O. Garay, F.E. Karasz, J. Polym. Sci. A: Polym. Chem. 30 (1992) 2233–2240.
[95] B.R. Cho, M.S. Han, Y.S. Suh, K.J. Oh, S.J. Jeon, J. Chem. Soc.: Chem. Commun. 6 (1993) 564–566.
[96] B.R. Cho, Y.K. Kim, M.S. Han, Macromolecules 31 (1998) 2098–2106.
[97] B.R. Cho, T.H. Kim, Y.K. Kim, N.S. Kim, Macromolecules 32 (1999) 3583–3589.
[98] B.R. Cho, T.H. Kim, K.H. Son, Y.K. Kim, Y.K. Lee, S.J. Jeon, Macromolecules 33 (2000) 8167–8172.
[99] J. Wiesecke, M. Rehahn, Angew. Chem. Int. Ed. 42 (2003) 567.
[100] J. Wiesecke, M. Rehahn, Macromol. Rapid Commun. 28 (2007) 188–193.
[101] T. Schwalm, M. Rehahn, Macromolecules 40 (2007) 3921–3928.
[102] T. Schwalm, J. Wiesecke, S. Immel, M. Rehahn, Macromolecules 40 (2007) 8842–8854.
[103] J. Wiesecke, M. Rehahn, Macromol. Rapid Commun. 28 (2007) 78–83.
[104] T. Schwalm, J. Wiesecke, S. Immel, M. Rehahn, Macromol. Rapid Commun. 30 (2009) 1295–1322.
[105] H. Becker, H. Spreitzer, K. Ibrom, W. Kreuder, Macromolecules 32 (1999) 4925–4932.
[106] N. Vilbrandt, Poly(p-phenylen vinylen)e nach Gilch: Konstitutions- und Morphologieeinflüsse auf die Emissionsfarbe und das Ermüdungsverhalten in organischen LEDs (Ph.D. thesis), Technische Universität Darmstadt, Chemistry Department, 2013.
[107] B. Thieke, Makromolekulare Chemie: Eine Einführung, Wiley-VCH, Weinheim, 2005.
[108] K.Z. Xing, N. Johansson, Adv. Mater. 9 (1997) 1027.
[109] T. Schwalm, M. Rehahn, Macromol. Rapid Commun. 29 (2008) 207–213.
[110] K. Ellmer, Nat. Photonics 6 (2012) 809–817.
[111] D.S. Ginley, H. Hosono, D.C. Paine, Handbook of Transparent Conductors, Springer, New York, 2010.
[112] C.G. Granqvist, Sol. Energy Mater. Sol. Cells 91 (2007) 1529–1598.
[113] K. Ellmer, A. Klein, B. Rech, Transparent Conductive Zinc Oxide: Basics and Applications in Thin Film Solar Cells, Springer-Verlag, Berlin, Heidelberg, 2008.
[114] L.S. Hung, C.H. Chen, Mater. Sci. Eng. R: Rep. 39 (2002) 143–222.
[115] J.C.C. Fan, J.B. Goodenough, J. Appl. Phys. 48 (1977) 3524–3531.
[116] I. Hamberg, C.G. Granqvist, J. Appl. Phys. 60 (1986) R123–R159.
[117] Y. Gassenbauer, A. Klein, J. Phys. Chem. B 110 (2006) 4793–4801.
[118] Y. Gassenbauer, R. Schafranek, A. Klein, S. Zafeiratos, M. Haevecker, A. Knop-Gericke, R. Schloegl, Phys. Rev. B 73 (2006) 245312.
[119] A. Klein, J. Am. Ceram. Soc. 96 (2013) 331–345.
[120] A. Schleife, J.B. Varley, F. Fuchs, C. Roedl, F. Bechstedt, P. Rinke, A. Janotti, C.G.V. de Walle, Phys. Rev. B 83 (2011) 035116.
[121] P. Erhart, A. Klein, R.G. Egdell, K. Albe, Phys. Rev. B 75 (2007) 153205.
[122] K. Irmscher, M. Naumann, M. Pietsch, Z. Galazka, R. Uecker, T. Schulz, R. Schewski, M. Albrecht, R. Fornari, Phys. Stat. Solid. A 211 (2014) 54–58.
[123] G. Frank, H. Koestlin, Appl. Phys. A 27 (1982) 197–206.
[124] N. Yamada, I. Yasui, Y. Shigesato, H. Li, Y. Ujihira, K. Nomura, Japan. J. Appl. Phys. 39 (2000) 4158–4163.
[125] G.B. Gonzáez, T.O. Mason, J.P. Quintana, O. Warschkow, D.E. Ellis, J.-H. Hwang, J.P. Hodges, J. Appl. Phys. 96 (2004) 3912–3920.
[126] R.B.H. Tahar, T. Ban, Y. Ohya, Y. Takahashi, J. Appl. Phys. 83 (1998) 2631–2645.
[127] H. Ohta, M. Orita, M. Hirano, H. Tanji, H. Kawazoe, H. Hosono, Appl. Phys. Lett. 76 (2000) 2740–2742.
[128] N. Preissler, O. Bierwagen, A.T. Ramu, J.S. Speck, Phys. Rev. B 88 (2013) 085305.
[129] S.B. Zhang, J.E. Northrup, Phys. Rev. Lett. 67 (1991) 2339–2342.
[130] P. Erhart, A. Klein, K. Albe, Phys. Rev. B 72 (2005) 085213.
[131] S. Lany, A. Zunger, Phys. Rev. Lett. 98 (2007) 045501.
[132] P. Ágoston, K. Albe, Phys. Chem. Chem. Phys. 11 (2009) 3226–3232.
[133] S. Lany, A. Zakutayev, T.O. Mason, J.F. Wager, K.R. Poeppelmeier, J.D. Perkins, J.J. Berry, D.S. Ginley, A. Zunger, Phys. Rev. Lett. 108 (2012) 016802.
[134] P. Ágoston, K. Albe, R.M. Nieminen, M.J. Puska, Phys. Rev. Lett. 103 (2009) 245501.
[135] P. Ágoston, C. Koerber, A. Klein, M.J. Puska, R.M. Nieminen, K. Albe, J. Appl. Phys. 108 (2010) 053511.
[136] S.B. Zhang, S.-H. Wei, A. Zunger, J. Appl. Phys. 83 (1998) 3192–3196.
[137] W. Walukiewicz, Physica B 302–303 (2001) 123–134.
[138] J. Robertson, S.J. Clark, Phys. Rev. B 83 (2011) 075205.
[139] G.P. Wirtz, H.P. Takiar, J. Am. Ceram. Soc. 64 (1981) 748–752.
[140] J. Berger, I. Riess, D.S. Tannhauser, Solid State Ionics 15 (1985) 225–231.
[141] Y. Ikuma, T. Murakami, J. Electrochem. Soc. 143 (1996) 2698–2701.
[142] Y. Ikuma, M. Kamiya, N. Okumura, I. Sakaguchi, H. Haneda, Y. Sawada, J. Electrochem. Soc. 145 (1998) 2910–2913.
[143] B. Kamp, R. Merkle, J. Maier, Sens. Actuators B 77 (2001) 534–542.
[144] B. Kamp, R. Merkle, R. Lauck, J. Maier, J. Solid State Chem. 178 (2005) 3027–3039.
[145] P. Ágoston, K. Albe, Phys. Rev. B 81 (2010) 195205.
[146] P. Erhart, K. Albe, Phys. Rev. B 73 (2006) 115207.
[147] P. Erhart, K. Albe, Appl. Phys. Lett. 88 (2006) 201918.
[148] P. Ágoston, Point defect and surface properties of $In_2O_3$ and $SnO_2$: a comparative study by first-principles methods (Ph.D. thesis), Technische Universität Darmstadt, Materials Science Department, 2011.
[149] M.V. Hohmann, A. Wachau, A. Klein, Solid State Ionics (2013), http://dx.doi.org/10.1016/j.bbr.2011.03.031.
[150] H. Ishii, K. Sugiyama, E. Ito, K. Seki, Adv. Mater. 11 (1999) 605–625.
[151] M. Fahlman, A. Crispin, X. Crispin, S.K.M. Henze, M.P. de Jong, W. Osikowicz, C. Tengstedt, W.R. Salaneck, J. Phys.: Condens. Matter 19 (2007) 183202.
[152] A. Klein, Thin Solid Films 520 (2012) 3721–3728.
[153] J.S. Kim, M. Granström, R.H. Friend, N. Johansson, W.R. Salaneck, R. Daik, W.J. Feast, J. Appl. Phys. 84 (1998) 6859–6870.
[154] M.G. Mason, L.S. Hung, C.W. Tang, S.T. Lee, K.W. Wong, M. Wang, J. Appl. Phys. 86 (1999) 1688–1692.
[155] X.M. Ding, L.M. Hung, L.F. Cheng, Z.B. Deng, X.Y. Hou, C.S. Lee, S.T. Lee, Appl. Phys. Lett. 76 (2000) 2704–2706.
[156] K. Sugiyama, H. Ishii, Y. Ouchi, K. Seki, J. Appl. Phys. 87 (2000) 295–298.
[157] M. Ishii, T. Mori, H. Fujikawa, S. Tokito, Y. Taga, J. Lumin. 87–89 (2000) 1165–1167.
[158] A. Klein, C. Körber, A. Wachau, F. Säuberlich, Y. Gassenbauer, R. Schafranek, S.P. Harvey, T.O. Mason, Thin Solid Films 518 (2009) 1197–1203.
[159] A. Klein, C. Körber, A. Wachau, F. Säuberlich, Y. Gassenbauer, S.P. Harvey, D.E. Proffit, T.O. Mason, Materials 3 (2010) 4892–4914.
[160] R.K. Swank, Phys. Rev. 153 (1967) 844–849.
[161] M. Batzill, U. Diebold, Prog. Surf. Sci. 79 (2005) 47–154.
[162] P. Ágoston, K. Albe, Surf. Sci. 605 (2011) 714–722.
[163] K. Rachut, C. Koerber, J. Broetz, A. Klein, Phys. Stat. Solid. A (2014), http://dx.doi.org/10.1002/pssa.201330367.
[164] J. Goniakowski, F. Finocchi, C. Noguera, Rep. Prog. Phys. 71 (2008) 016501.
[165] P.W. Tasker, J. Phys. C 12 (1979) 4977.
[166] P. Ágoston, K. Albe, Phys. Rev. B 84 (2011) 045311.
[167] A. Walsh, C.R.A. Catlow, J. Mater. Chem. 20 (2010) 10438–10444.
[168] O. Bierwagen, J.S. Speck, J. Appl. Phys. 107 (2010) 113519.
[169] M.V. Hohmann, P. Ágoston, A. Wachau, T.J.M. Bayer, J. Broetz, K. Albe, A. Klein, J. Phys.: Condens. Matter 23 (2011) 334203.
[170] Y. Gassenbauer, A. Wachau, A. Klein, Phys. Chem. Chem. Phys. 11 (2009) 3049–3054.
[171] K. Ellmer, T. Welzel, J. Mater. Res. 27 (2012) 765–779.
[172] A. Klein, Appl. Phys. Lett. 77 (2000) 2009–2011.
[173] C. Jonda, A.B.R. Mayer, U. Stolz, A. Elschner, A. Karbach, J. Mater. Sci. 35 (2000) 5645–5651.
[174] T. Minami, T. Kakumu, S. Takata, J. Vacuum Sci. Technol. A 14 (1996) 1704–1708.
[175] M.P. Taylor, D.W. Readey, M.F.A.M. van Hest, C.W. Teplin, J.L. Alleman, M.S. Dabney, L.M. Gedvilas, B.M. Keyes, B. To, J.D. Perkins, D.S. Ginley, Adv. Funct. Mater. 18 (2008) 3169–3178.
[176] E.M. Hopper, Q. Zhu, J. Gassmann, A. Klein, T.O. Mason, Appl. Surf. Sci. 264 (2013) 811–815.

[177] S. Tokito, K. Noda, Y. Taga, J. Phys. D: Appl. Phys. 29 (1996) 2750–2753.
[178] X.J. Xu, G. Yu, Y.Q. Liu, D.B. Zhu, Displays 27 (2006) 24–34.
[179] M. Kroeger, S. Hamwi, J. Meyer, T. Riedl, W. Kowalsky, A. Kahn, Appl. Phys. Lett. 95 (2009) 123301.
[180] T. Matsushima, G.H. Jin, H. Murata, J. Appl. Phys. 104 (2008) 054501.
[181] S.B. Adler, X.Y. Chen, J.R. Wilson, J. Catal. 245 (2007) 91–109.
[182] R. Merkle, J. Maier, Angew. Chem. Int. Ed. 47 (2008) 3874–3894.
[183] J. Jamnik, B. Kamp, R. Merkle, J. Maier, Solid State Ionics 150 (2002) 157–166.
[184] C. Koerber, A. Wachau, P. Ágoston, K. Albe, A. Klein, Phys. Chem. Chem. Phys. 13 (2011) 3223–3226.
[185] F. Neumann, Y.A. Genenko, C. Melzer, S.V. Yampolskii, H. von Seggern, Phys. Rev. B 75 (2007) 205322.
[186] Y. Kurosaka, N. Tada, Y. Ohmori, K. Yoshino, Elect. Eng. Jpn. 132 (2000) 1373–1376.
[187] T.J.M. Bayer, A. Wachau, A. Fuchs, J. Deuermeier, A. Klein, Chem. Mater. 24 (2012) 4503–4510.
[188] V. Choong, Y. Park, Y. Gao, B. Hsieh, C. Tang, Macromol. Symp. 125 (1997) 83–97.
[189] W. Bruetting, J. Frischeisen, T. Schmidt, B.J. Scholz, C. Mayr, Phys. Stat. Solid. A 210 (2013) 44–65.
[190] S. Karg, M. Meier, W. Riess, J. Appl. Phys. 82 (1997) 1951–1960.
[191] L. Bozano, S.A. Carter, J.C. Scott, G.G. Malliaras, P.J. Brock, Appl. Phys. Lett. 74 (1999) 1132–1134.
[192] M. Redecker, D.D.C. Bradley, M. Inbasekaran, E.P. Woo, Appl. Phys. Lett. 73 (1998) 1565–1567.
[193] S. Naka, H. Okada, H. Onnagawa, T. Tsutsui, Appl. Phys. Lett. 76 (2000) 197–199.
[194] P.W.M. Blom, M.J.M. deJong, J.J.M. Vleggaar, Appl. Phys. Lett. 68 (1996) 3308–3310.
[195] Y. Zhang, B. de Boer, P.W.M. Blom, Phys. Rev. B 81 (2010) 085201.
[196] M. Kuik, J. Vandenbergh, L. Goris, E.J. Begemann, L. Lutsen, D.J.M. Vanderzande, J.V. Manca, P.W.M. Blom, Appl. Phys. Lett. 99 (2011) 183305.
[197] H. Scher, M.F. Shlesinger, J.T. Bendler, Phys. Today 44 (1991) 26.
[198] H. Scher, E.W. Montroll, Phys. Rev. B 12 (1975) 2455–2477.
[199] H.C.F. Martens, P.W.M. Blom, H.F.M. Schoo, Phys. Rev. B 91 (2000) 7489–7493.
[200] H.C.F. Martens, J.N. Huiberts, P.W.M. Blom, Appl. Phys. Lett. 77 (2000) 1852–1854.
[201] H. Baessler, Phys. Stat. Solid. B: Basic Res. 175 (1993) 15–56.
[202] E. Lehtonen, A. Gassmann, 2013 (unpublished results).
[203] S.A. VanSlyke, C.H. Chen, C.W. Tang, Appl. Phys. Lett. 69 (1996) 2160–2162.
[204] C. Fery, B. Racine, D. Vaufrey, H. Doyeux, S. Cina, Appl. Phys. Lett. 87 (2005) 213502–213504.
[205] T.B. Canzler, M. Burghart, S. Murano, J. Blochwitz-Nimoth, B. D'Andrade, M. Hack, J.J. Brown, Proc. SPIE 6333 (2006) 633311–633321.
[206] H. Nakanotani, K. Masui, J. Nishide, T. Shibata, C. Adachi, Sci. Rep. 3 (2127) (2013) 1–6.
[207] R. Savikoski, O. Pekkola, A. Gassmann, 2012 (unpublished results).
[208] R. Friend, R. Gymer u.a., Nature 397 (1999) 121–128.
[209] A. Koehler, H. Baessler, Mater. Sci. Eng. R 66 (2009) 71–109.
[210] V. Cleave, G. Yahioglu, P. Le Barny, R. Friend, N. Tessler, Adv. Mater. 11 (1999) 285–288.
[211] J.M. Lupton, I.D.W. Samuel, M.J. Frampton, R. Beavington, P.L. Burn, Adv. Funct. Mater. 11 (2001) 287–294.
[212] G. Schwartz, S. Reineke, T.C. Rosenow, K. Walzer, K. Leo, Adv. Funct. Mater. 19 (2009) 1319–1333.
[213] H. Yersin, A.F. Rausch, R. Czerwieniec, T. Hofbeck, T. Fischer, Coord. Chem. Rev. 255 (2011) 2622–2652.
[214] R. Seifert, I.R. de Moraes, S. Scholz, M.C. Gather, B. Luessem, K. Leo, Org. Electron. 14 (2013) 115–123.
[215] P.E. Burrows, S.R. Forrest, T.X. Zhou, L. Michalski, Appl. Phys. Lett. 76 (2000) 2493–2495.
[216] C. Yun, J. Lee, J. Lee, B. Lussem, F. Ventsch, K. Leo, M.C. Gather, Appl. Phys. Lett. 101 (2012) 243303.
[217] H. Burrows, J. de Melo, C. Serpa, L. Arnaut, A. Monkman, I. Hamblett, S. Navaratnam, J. Chem. Phys. 115 (2001) 9601–9606.
[218] P.F. Barbara, A.J. Gesquiere, Y.J. Lee, J. Yu, Acc. Chem. Res. 38 (2005) 602–610.
[219] F. Laquai, C. Im, A. Kadashchuk, H. Baessler, Chem. Phys. Lett. 375 (2003) 286.
[220] P. Heremans, D. Cheyns, B.P. Rand, Acc. Chem. Res. 42 (2009) 1740–1747.
[221] O. Pekkola, A. Gassmann, F. Etzold, F. Laquai, H. von Seggern, Phys. Stat. Solid. A 211 (2014) 2035–2039.
[222] C. Gaerditz, A. Winnacker, F. Schindler, R. Paetzold, Appl. Phys. Lett. 90 (2007) 103506.
[223] J. Sheats, H. Antoniadis, M. Hueschen, W. Leonard, J. Miller, R. Moon, D. Roitman, A. Stocking, Science 273 (1996) 884–888.
[224] A. Sperlich, H. Kraus, C. Deibel, H. Blok, J. Schmidt, V. Dyakonov, J. Phys. Chem. B 115 (2011) 13513–13518.
[225] H. Low, Thin Solid Films 413 (2002) 160–166.
[226] B.H. Cumpston, I.D. Parker, K.F. Jensen, J. Appl. Phys. 81 (1997) 3716.
[227] R. Coehoorn, P.A. Bobbert, Phys. Stat. Solid. A 209 (2012) 2354–2377.
[228] A. Walker, A. Kambili, S. Martin, J. Phys.: Condens. Matter 14 (2002) 9825–9876.
[229] M. Kuik, G.-J.A.H. Wetzelaer, H.T. Nicolai, N.I. Craciun, D.M. De Leeuw, P.W.M. Blom, Adv. Mater. 26 (2014) 512–531.
[230] D. Monroe, Phys. Rev. Lett. 54 (1985) 146–149.
[231] S.D. Baranovskii, T. Faber, F. Hensel, P. Thomas, J. Phys.: Condens. Matter 9 (1997) 2699–2706.
[232] V.I. Arkhipov, U. Wolf, H. Baessler, Phys. Rev. B 59 (1999) 7514–7520.
[233] S.D. Baranovskii, Phys. Stat. Solid. B: Basic Solid Stat. Phys. 251 (2014) 487–525.
[234] V.I. Arkhipov, A.I. Rudenko, Philos. Mag. B 45 (1982) 189–207.
[235] N. Mott, Conduction in Non-Crystalline Solids, Clarendon Press, Oxford, 1987.
[236] V.I. Arkhipov, H. von Seggern, E.V. Emelianova, Appl. Phys. Lett. 83 (2003) 5074–5076.
[237] N.W. Ashcroft, N.D. Mermin, Solid State Physics, Thompson Learning, Florence, 1976.
[238] F. Neumann, Y.A. Genenko, H. von Seggern, J. Appl. Phys. 99 (2006) 013704.
[239] Y. Roichman, N. Tessler, Appl. Phys. Lett. 80 (2002) 1948.
[240] F. Neumann, Y.A. Genenko, R. Schmechel, H. von Seggern, Synth. Met. 150 (2005) 291–296.
[241] M. Lampert, P. Mark, Current Injection in Solids, Academic Press, 1970.
[242] B.K. Crone, P.S. Davids, I.H. Campbell, D.L. Smith, J. Appl. Phys. 84 (1998) 833–842.
[243] F. Neumann, Y.A. Genenko, C. Melzer, H. von Seggern, J. Appl. Phys. 100 (2006) 084511.
[244] S.V. Yampolskii, Y.A. Genenko, C. Melzer, K. Stegmaier, H. von Seggern, J. Appl. Phys. 104 (2008) 073719.
[245] S. Sze, K.K. Ng, Physics of Semiconductor Devices, 3rd ed., Wiley Interscience, 2007.
[246] Y.A. Genenko, S.V. Yampolskii, C. Melzer, K. Stegmaier, H. von Seggern, Phys. Rev. B 81 (2010) 125310.
[247] C. Crowell, S. Sze, Solid-State Electron. 9 (1966) 1035–1048.
[248] P.W.M. Blom, M.C.J.M. Vissenberg, Mater. Sci. Eng. R: Rep. 27 (2000) 53–94.
[249] S.V. Yampolskii, Y.A. Genenko, C. Melzer, H. von Seggern, J. Appl. Phys. 109 (2011) 073722.
[250] V.I. Arkhipov, P. Heremans, E.V. Emelianova, G.J. Adriaenssens, Appl. Phys. Lett. 79 (2001) 4154.
[251] V.R. Nikitenko, H. Heil, H. von Seggern, J. Appl. Phys. 94 (2003) 2480–2485.
[252] W.F. Pasveer, J. Cottaar, C. Tanase, R. Coehoorn, P.A. Bobbert, P.W.M. Blom, D.M. de Leeuw, M.A.J. Michels, Phys. Rev. Lett. 94 (2005) 206601.
[253] S.L.M. van Mensfoort, R. Coehoorn, Phys. Rev. B 78 (2008) 085207.
[254] M. Bouhassoune, S.L.M. van Mensfoort, P.A. Bobbert, R. Coehoorn, Org. Electron. 10 (2009) 437–445.